REVIEW

Spinel integrated layered oxide cathodes for sodium-ion batteries: suppressing phase transitions, enhancing air stability, and accelerating Na⁺ transport

Rui Li,[a] Yan-Jiang Li,[*b] Neng-Hua Xu,[a] Bing-Bing Chen,[a] Hai-Yan Hu,[a] Yan-Fang Zhu[*a] and Yao Xiao [iD] [*a]

Sodium layered transition metal oxides (Na_xTMO_2), as the key cathode material for sodium-ion batteries, are still limited by the core issues such as irreversible phase transitions, air instability, and sluggish kinetics, generally leading to rapid performance degradation. The spinel-type (AB_2O_4) material, with its excellent structural stability and fast ion diffusion channels, provides an effective solution to overcome the challenges faced by Na_xTMO_2 through incorporation. In this study, we systematically review the construction methods of layered/spinel heterostructures and elucidate the core role of the spinel phase in optimizing the properties of Na_xTMO_2 cathodes. Subsequently, we discuss and integrate representative strategies for mitigating irreversible phase transitions, enhancing air stability, and accelerating Na⁺ transport kinetics, including multiphase composites, spinel sublayer coating and spinel coating strategies, *etc*. Finally, this review summarizes the challenges faced in spinel regulation strategies and provides corresponding research directions, while also looking forward to the development of layered/spinel heterostructures in various fields in the future. We believe that this analysis will inspire more theoretical understanding and practical guidance for the development of Na_xTMO_2 cathodes.

1 Introduction

The extensive use of conventional fossil fuels has posed severe environmental challenges, making the development and application of renewable energy imperative.[1–3] Over the past decades, sustainable energy technologies such as wind, solar, and hydropower have been widely deployed.[4,5] Nevertheless, these renewable energy sources often exhibit inherent intermittency and limitations in application scenarios, which hinder their widespread applications.[6–8] Therefore, the research and development of highly efficient energy storage technologies have become increasingly urgent. Owing to its rapid response and flexible site selection, electrochemical energy storage is currently one of the most suitable options for renewable energy development. Lithium-ion batteries (LIBs) have received significant attention over the past decades due to their high energy density and long cycling life.[9–11] However, the scarcity of lithium resources leads to prominent price fluctuations and greatly constrains the development of the downstream industrial chain.[12] Sodium is a low-cost and abundant resource, with

its abundance exceeding that of lithium by more than 1000 times (Fig. 1a), making sodium-ion batteries (SIBs) the most promising supplement to LIBs.[13–15] Compared with LIBs, SIBs are more advantageous in terms of environmental compatibility and safety (Fig. 1b).[14–18]
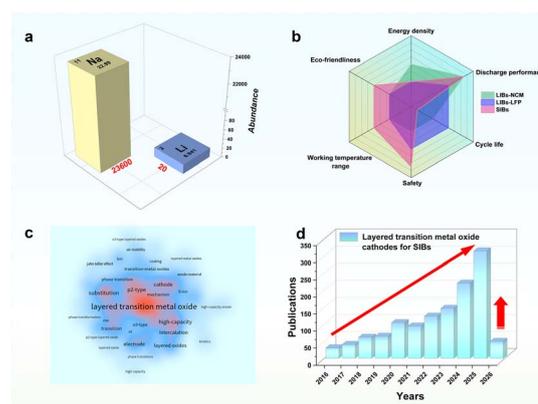

Fig. 1 (a) Comparison of lithium and sodium resource abundances in the earth's crust. (b) Comparison of the performance of LIBs with different cathodes and SIBs. (c) Research hotspots of Na_xTMO_2 for SIBs (data were collected from the Web of Science Core Collection, Mar. 2026). (d) The number of articles relevant to Na_xTMO_2 (data were collected from the Web of Science Core Collection, Mar. 2026).

aCollege of Chemistry and Materials Engineering, Wenzhou University, Wenzhou, Zhejiang, 325035, P. R. China. E-mail: xiaoyao@wzu.edu.cn; yanfangzhu@wzu.edu.cn

bKey Laboratory of Spin Electron and Nanomaterials of Anhui Higher Education Institutes, Suzhou University, Suzhou 234000, China. E-mail: yjli@ahszu.edu.cn

Additionally, under extreme conditions such as overcharging/overdischarging and severe temperature fluctuations, SIBs exhibit greater tolerance.[19–21] This wide-temperature-range adaptability and intrinsic safety endow SIBs with excellent operational reliability in harsh environments, offering a promising solution for energy storage applications under extreme climate conditions.[22–26] As a key component that determines the performance of SIBs, layered transition metal oxide cathodes (Na_xTMO_2, $0 < x < 1$, TM = Fe, Mn, Ni, Co, *etc.*) have become a research focus due to their high theoretical capacity, appropriate redox potential, and facile synthesis.[27–31] We retrieved literature on Na_xTMO_2 from the Web of Science Core Collection database covering 2016 to 2026 and present a hotspot map (Fig. 1c).

As seen, Na_xTMO_2 has emerged as a major research focus due to its outstanding electrochemical performance, highlighting its strong potential as a promising technology for large-scale energy storage applications.[32–35] Structurally, Na_xTMO_2 is commonly classified according to the Na^+ coordination environment within the lattice and the stacking sequence of the $(TMO_2)_n$ slabs, giving rise to two representative phase types: P2-type ($0.6 < x < 0.8$) and O3-type ($0.8 < x < 1$).[36] "P" indicates that Na^+ occupies trigonal prismatic sites, whereas "O" denotes octahedral sites; the numeral specifies the number of transition metal (TM) layers within one repeating stacking unit.[37,38] Benefiting from relatively open diffusion pathways, P2-type materials generally exhibit faster Na^+ diffusion kinetics and superior structural stability.[33,39] In contrast, owing to their high Na stoichiometry, O3-type materials demonstrate high theoretical specific capacity and initial coulombic efficiency, offering better compatibility for full-cell construction.[40–42] Correspondingly, the number of research publications regarding Na_xTMO_2 has shown a continuous increase (Fig. 1d) over the past decade, reflecting growing interest in high-performance cathode materials.

Unfortunately, Na_xTMO_2 cathodes commonly suffer from severe challenges such as detrimental phase transitions, poor air stability, and slow ion transport kinetics (Fig. 2), which greatly limit their large-scale applications.[43–47] Specifically, the TM layer generally undergoes interslab gliding induced by electrostatic repulsion within the Na layer upon Na^+ extraction/insertion, leading to partially reversible phase transitions.[48–52]
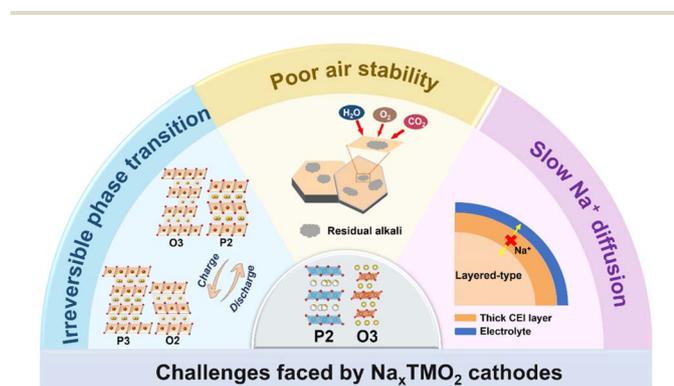
The O3-type Na_xTMO_2 typically undergoes complicated phase transitions such as O3 → O′3 (monoclinic phase), O3 → P3, and/or O3 → P′3, while P2-type materials are prone to undergo P2 → OP4 and/or P2 → O2 transitions.[53–56] These phase transitions are accompanied by substantial lattice volume change, generating stress concentration and ultimately resulting in structural collapse and capacity fade.[57–59] In addition, because of the high concentration of residual sodium compounds on the surface of Na_xTMO_2 particles, exposure to air triggers spontaneous reactions with moisture and CO_2, producing alkaline by-products that cause particle surface degradation and reduce the active Na^+ concentration.[60,61] Specifically, for the O3-type Na_xTMO_2, after exposure to moisture, the spontaneous reaction following $NaTMO_2 + xH_2O \rightarrow Na_{1-x}H_xTMO_2 + xNaOH$ generates NaOH, which then rapidly reacts with CO_2 in air owing to the high Na content at the interface, forming alkaline residues such as Na_2CO_3 and $NaHCO_3$.[62–68] Regarding the P2 phase, the larger interlayer spacing of prismatic coordination sites allows the H_2O and CO_2 molecules to intercalate into the layered lattice, triggering the reaction of $NaTMO_2 + xH_2O + CO_2 \rightarrow Na_{1-x}H_x$-$TMO_2 + NaHCO_3$, which leads to swelling of the layered structure and the formation of surface deposits.[69–72] Compared to Li^+, Na^+ possesses a larger ionic radius (1.02 Å *vs.* 0.76 Å), a higher atomic mass (23 g mol^{-1} *vs.* 6.9 g mol^{-1}), and a higher redox potential in the Na^+/Na couple.[73,74] These intrinsic properties result in lower energy densities on both a volumetric and gravimetric basis, slower reaction kinetics, and reduced cycle life compared to those of LIBs.[73,74] Structurally, the octahedral channels occupied by Na^+ in the O3-type phase are narrow and prone to blockage, whereas the P2-type framework tends to undergo layer slipping and phase transitions under high voltages.[75–79] During electrochemical cycling, these adverse structural evolutions and lattice deformations (such as Jahn–Teller distortion) further compress the Na^+ diffusion channels, resulting in poor rate capability.[80,81] To overcome the inherent limitations of Na_xTMO_2, previous research has developed various interface and structural modulation strategies.[82] Among them, layered/spinel composite structures have been widely explored. The spinel phase, with its unique three-dimensional (3D) ion diffusion channels, a robust lattice framework, and excellent air stability, serves as an effective stabilizer to address the key challenges faced by Na_xTMO_2.[83,84]

The spinel structure (AB_2O_4, space group $Fd\bar{3}m$) has attracted considerable attention in SIBs due to its unique 3D framework and wide ion diffusion channels.[85,86] In this structure, the A site is typically occupied by alkali metal ions, while the B site is filled with TM ions, together forming a crystal configuration with excellent structural stability.[87,88] Furthermore, the AB_2O_4 family also includes post-spinel structures, which can transform from the spinel phase under high pressure, such as $CaFe_2O_4$-type $NaMn_2O_4$ and $NaVSnO_4$.[89] In a typical spinel phase, A-site ions preferentially occupy the tetrahedral $8a$ sites, and B-site ions reside in the octahedral $16d$ sites. The BO_6 octahedra form a 3D network framework and provide transport channels for ion migration.[90,91] Due to its rigid crystal framework and internal open space that supports rapid Na^+ transport, the spinel structure exhibits several advantages complementary to layered

Fig. 2 The challenges faced by Na_xTMO_2 cathodes.

oxides in SIBs: (i) the 3D Na^+ migration channels generally correspond to low diffusion energy barriers, facilitating high-rate charging and discharging.[92] (ii) The TM-O framework helps minimize lattice strain and overall volume changes during Na^+ (de)intercalation, thereby alleviating stress concentration and suppressing microcrack evolution during cycling.[88] Therefore, the spinel-layered oxide coexisting configuration can integrate their structural advantages to construct high-performance cathodes. Herein, the spinel phase will not only shorten the diffusion distance and accelerate Na^+ transport but also stabilize the layered lattice during cycling.[91]

As shown in Fig. 3, the spinel structure has been used to reinforce the phase stability of Na_xTMO_2 over the past decade. Initially, research primarily focused on improving the electrochemical properties of Na_xTMO_2 by coupling it with a spinel phase.[93,94] Then, with the widespread adoption of *in situ* characterization techniques, the functional mechanisms of the spinel phase were further elucidated, and more studies have aimed at the coordinated optimization of phase transitions and ion transport kinetics.[95–97] In recent years, spinel/layered composite structures have been designed to regulate interfacial stability and suppress lattice oxygen escape, and this concept has been extended to high-entropy systems, leading to significantly improved performance.[98–100] Therefore, this work provides an overview of the unique advantages of spinel assistance in improving the properties of Na_xTMO_2 cathodes, primarily including alleviating irreversible phase transitions, stabilizing lattice oxygen and TM ions, and accelerating Na^+ (de) intercalation kinetics. The intrinsic regulatory mechanisms between the spinel and layered phases are systematically elucidated. Finally, we prospectively discuss the construction methods and recycling techniques of spinel/layered heterogeneous architectures. We believe that this review will provide valuable insights into the rational design of spinel/layered phase composite structures, thereby accelerating the development of high-performance Na_xTMO_2 cathodes.

2 Construction of layered/spinel heterostructures

P2-type ($P6_3/mmc$) and O3-type ($R\bar{3}m$) layered oxides differ fundamentally in oxygen stacking sequences and Na coordination environments. P2 structures exhibit ABBA-type oxygen stacking with prismatic Na coordination,[69,71,72] whereas O3 structures adopt ABC stacking with octahedral Na coordination.[101,102] In contrast, cubic spinel phases ($Fd\bar{3}m$) are constructed from a cubic close-packed oxygen framework. The TM ions within the spinel phases occupy octahedral and tetrahedral sites, forming 3D interconnected ion diffusion channels (Table 1).[103] Such comparable TM occupancies and TM–O bonds in the layered and spinel phases may provide firm bonding at the interface to build a stable heterogeneous phase configuration.

Table 1 Comparison of crystallographic structural parameters between P2, O3-type configurations and spinel phases

Structure	Space group	Oxygen stacking	Na coordination
P2	$P6_3/mmc$	ABBA	Prismatic
O3	$R\bar{3}m$	ABC	Octahedral
Spinel	$Fd\bar{3}m$	Cubic close-packed	Tetra./Octa. TM

J.R. Kim et al., *Chem. Mater.* **2015**, 27, 2546-2556

S.-H. Guo et al., *Nat. Commun.* **2017**, 8, 135

X.-J. Nie et al., *Electrochim. Acta* **2019**, 320, 134626

Y. Xiao et al., *Cell Rep. Phys. Sci.* **2021**, 2, 100547

J.-Y. Li et al., *Adv. Funct. Mater.* **2023**, 33, 2213215

N. Zhen et al., *Energy Stor. Mater.* **2025**, 74, 103971

2015 2016 2017 2018 2019 2020 2021 2022 2023 2024 2025

J. Zheng et al., *J. Electrochem. Soc.* **2016**, 163, A584-A591

C.-J. Deng et al., *Chem. Mater.* **2018**, 30, 8145-8154

Y.-F. Zhu et al., *Angew. Chem. Int. Ed.* **2020**, 59, 9299-9304

H.-Y. Hu et al., *Adv. Energy Mater.* **2022**, 12, 2201511

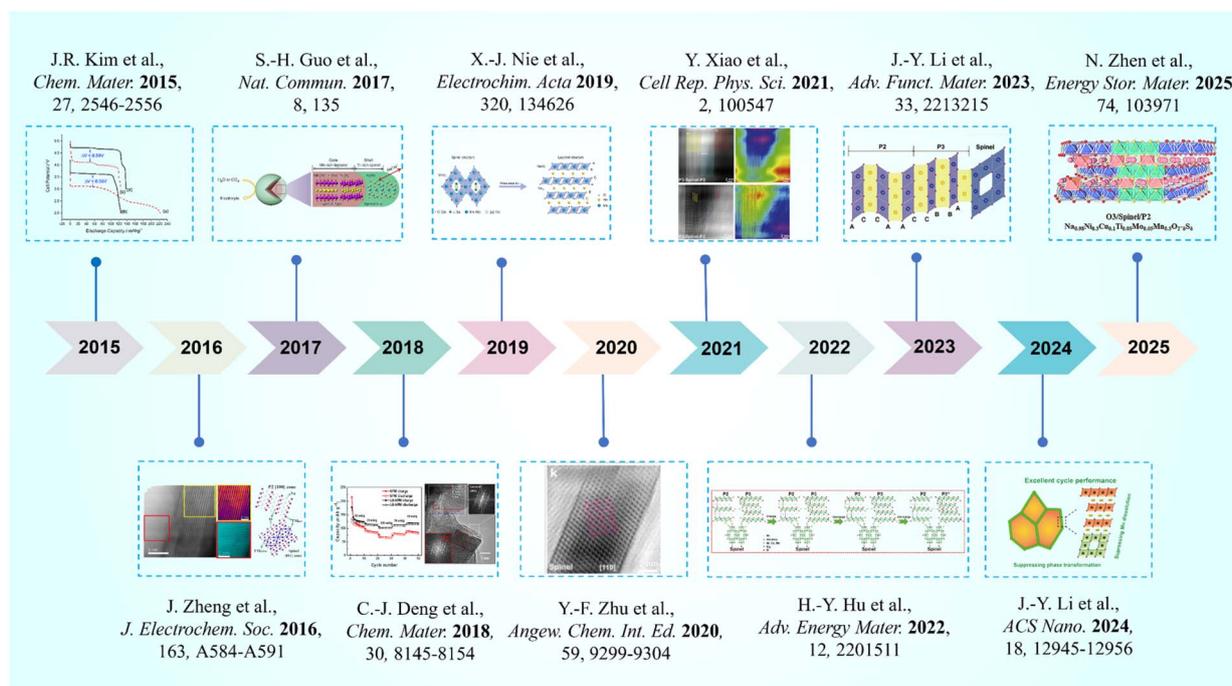J.-Y. Li et al., *ACS Nano.* **2024**, 18, 12945-12956

Fig. 3 The development of spinel engineering on layered oxide cathodes for SIBs.

In the layered/spinel composite configuration, the spinel phase serves as a surface coating layer or as a structural skeleton to support the layered lattice. The synthesis strategy largely determines the structural components and roles of the spinel phase. Currently, the synthesis methods (Fig. 4) for layered/spinel composite Na_xTMO_2 cathodes mainly include Li^+/Na^+ ion exchange, solid-state reaction, pulse-assisted low-temperature sintering (PLTS), quenching treatment, and liquid-phase reduction.

For the ion-exchange method, the spinel $LiMn_2O_4$ (LMO-S) is generally synthesized through solid-state sintering at first. Then, the LMO-S is charged to a high voltage (4.3 V $vs.$ Li/Li^+) to achieve delithiation composition in a Li half-cell system. Following disassembly and reassembly with a Na anode, spinel-type $NaMn_2O_4$ is produced upon discharge to 2 V ($vs.$ Na/Na^+).[104]

It is important to note that in $NaMn_2O_4$, Na^+ insertion triggers a partial spinel-to-layered transformation, during which Mn^{3+}/Mn^{4+} ions migrate from the 16d octahedral sites to the 16c sites in the cubic close-packed oxygen array, and the oxygen anions rearrange from cubic close packing to hexagonal close packing. Ultimately, a spinel-layered intergrowth composite is formed. However, this method involves complex steps and imposes certain requirements on the material system. For other spinel or non-Mn-based systems that do not undergo such a transformation, this method may not yield a similar intergrowth structure.

The conventional solid-state reaction method is the most frequently applied strategy to synthesize layered/spinel composite cathodes due to its operational simplicity.[105] Here, the elemental ratio and sintering conditions are key factors
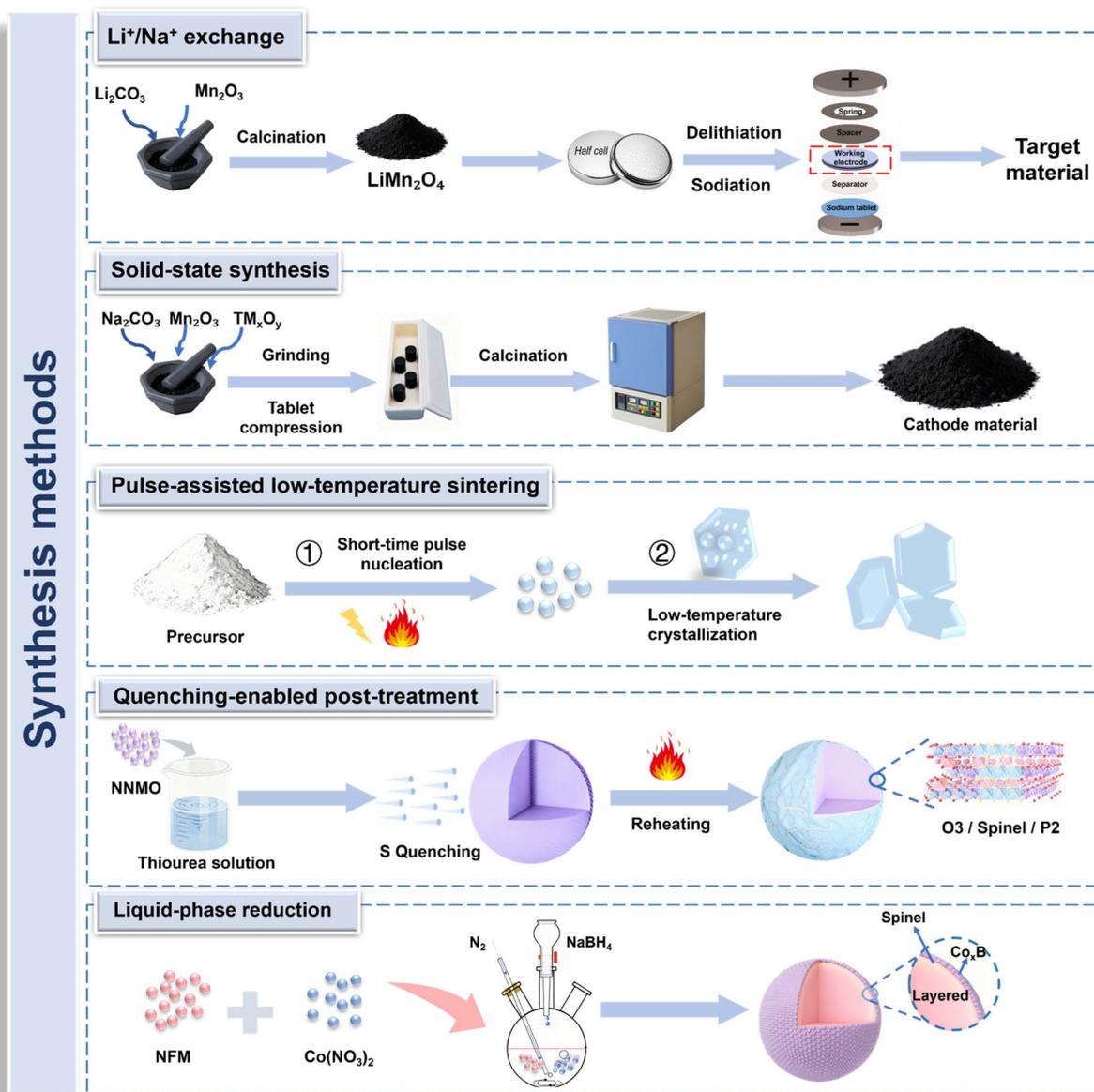

Fig. 4 Synthesis methods of layered/spinel heterostructure cathodes.

governing the final phase structure. An inappropriate element ratio may lead to impurity phases or result in defects in the spinel structure. Moreover, the radius of TM ions is required to match the size of tetrahedral/octahedral sites in the spinel phase.[106] Generally, the formation energy of the spinel phase is higher than that of the layered phase, which therefore requires a higher calcination temperature. A sufficient oxygen partial pressure plays a key role in determining the TM oxidation state, while the soaking time largely determines the crystallization of the spinel structure.[107] Notably, solid-state calcination can't accurately control the particle size and morphology of the as-prepared products, which makes it challenging to construct well-designed structures.

The PLTS method, which centers on using short-duration high-temperature pulses for rapid nucleation, can dramatically mitigate particle agglomeration. This is followed by low-temperature holding, allowing the nucleated particles to grow under milder conditions.[108] Meanwhile, oxygen vacancies (OVs) are introduced during the PLTS process, synergizing with spinel-like surface reconstruction. Specifically, the reduced particle size and lower agglomeration shorten the Na^+ diffusion pathway, while surface OVs enhance ionic transport. The induced spinel protective layer can suppress oxygen loss and interfacial corrosion. However, careful control of the PLTS pulse duration is required: an excessively long pulse may cause sintering and agglomeration, while an overly short pulse can hinder surface reconstruction.

After high-temperature sintering, quenching treatment is an efficient way to construct heterogeneous phases in the matrix. Through quenching treatment and subsequent secondary calcination, the target element can be doped into the layered lattice and then react with the bulk elements to form a spinel phase, which is located between layered phase structures, constructing a bridging framework to constrain phase transitions and alleviate stress.[98] It should be noted that these procedures require strict control of the thermal treatment parameters due to competitive growth among multiple phase structures governed by thermodynamic and kinetic processes.

Liquid-phase reduction methods feature homogeneous elemental distribution and the ability to coat heterogeneous species on the surface of the bulk phase, which can be used to build a spinel-like layer at the layered/spinel interface. This external spinel phase, with fast ion-transport pathways and a robust framework, can greatly enhance the rate capability and cycling stability of the as-prepared products.[109] Notably, this method is simple to operate and low-cost, requiring neither high-temperature sintering nor complex equipment, and is applicable to thermally unstable layered oxides.

In summary, the aforementioned methods with diverse characteristics are conducted as valid ways for constructing superior layered/spinel composite Na_xTMO_2 cathodes. Among the various methods currently used, considering the cost, operability, and environmental friendliness, the traditional solid-state synthesis and the PLTS are the most widely applicable and suitable for large-scale application.

3   Reinforcing performance *via* layered/spinel heterostructures

Owing to its excellent air tolerance and chemical inertness, the spinel phase has been confirmed to effectively improve the phase stability, air tolerance, and ion transport kinetics of Na_xTMO_2 cathodes.[110] Among the modification strategies for layered oxide cathode materials, surface coating and bulk doping are the two most common approaches. Traditional surface coating merely acts as a physical barrier; while it can mitigate electrolyte corrosion, it is less effective in inhibiting lattice oxygen loss within the bulk phase.[111,112] Bulk doping can modulate the electronic structure of the material, yet it cannot achieve precise regulation at the interfacial region.[113,114] Different from traditional surface coating and element component regulating, the spinel phase provides mechanical confinement for stabilizing the lattice oxygen. Its dense 3D structure anchors the layered framework, suppresses lattice distortion and interlayer sliding, and buffers internal stress during repeated Na^+ extraction/insertion.[107,109] This structural rigidity effectively mitigates TM ion migration, volume change, and crack propagation that often trigger oxygen release at high voltage states. In the following sections, we will systematically discuss how the spinel phase, through its unique structural and interfacial features, contributes to phase stability, air tolerance, and ion transport kinetics.

3.1   Suppressing phase transition

Layered structures generally undergo detrimental phase transformations such as P2 → O2, P2 → O′2, and P3 → O3′, especially at deeply (de)sodiated states, leading to electrochemical performance degradation.[115–120] Integrating a spinel phase provides a robust structural skeleton to suppress the harmful phase transitions of layered architectures. Specifically, spinel-assisted stabilization of Na_xTMO_2 can be implemented through three schematic routes (Fig. 5): (i) multiphase composite. By constructing multiphase configuration like P2/
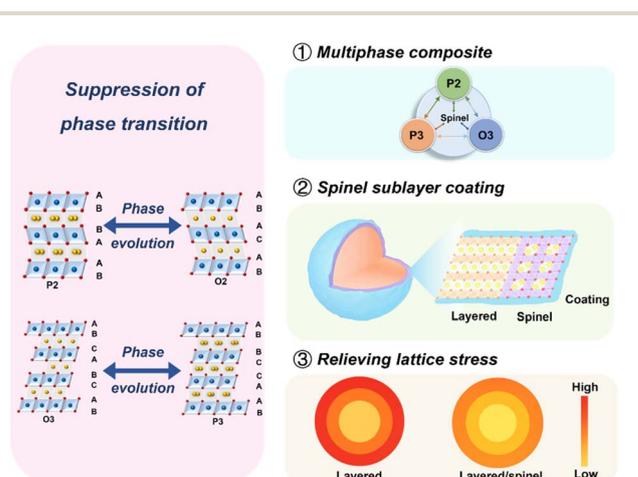

Fig. 5 Summary of enhanced structural properties for Na_xTMO_2 by integrating with spinel phases.

P3/O3/spinel structure, the spinel phase acts as a robust framework for mitigating the P2 → O2 and O3 ↔ P3 phase evolutions upon desodiation.[121] (ii) Spinel sublayer coating. The spinel interlayer is placed between the layered host and an outer coating layer, where the spinel layer serves as a transition layer to suppress surface reconstruction. (iii) Lattice-stress regulation. As shown in the stress distribution maps (Fig. 5), incorporating a spinel component can homogenize the internal stress field and reduce stress concentrations, which is critical for suppressing stress-driven structural degradation during cycling.[122]

It is worth noting that the spinel content also plays a critical role in the performance of layered oxide cathodes. Song *et al.*[123] constructed a triple-layer structure Na_2MoO_4/spinel/O3-type $NaNi_{1/3}Fe_{1/3}Mn_{1/3}O_2$ ($NaNi_{1/3}Fe_{1/3}Mn_{1/3}O_2$@NMO-X) by regulating the Mo content (1%, 2%, 3% and 5%). Among these, the sample modified with 2% Mo ($NaNi_{1/3}Fe_{1/3}Mn_{1/3}O_2$@NMO-2) manifested a uniform spinel interlayer with a thickness of approximately 3–4 nm, and exhibited the best durability (85.20% capacity retention *vs.* 81.98% (1%) and 83.53% (3%)). As reported by Nie *et al.*,[98] the O3/spinel/P2-$Na_{0.98}Ni_{0.3}Cu_{0.1}Ti_{0.05}Mo_{0.05}Mn_{0.5}O_{2-\delta}S_\delta$, with a spinel content of 6.06%, delivered significantly improved cycling stability (86.65% capacity retention after 200 cycles *vs.* 64.25% for the unmodified sample). Generally, the insufficient spinel content cannot exert the structural rigidity effectively, while an excessive content may sacrifice capacity. It is noteworthy that the critical threshold for spinel content often varies significantly among different material systems, making it difficult to summarize with a single unified value. Systematic screening and optimization are required based on the specific properties of the materials.

3.1.1 Multiphase composite. The spinel phase acts as a robust framework that pins TMO_6 interlayer gliding, thereby mitigating irreversible phase transitions during cycling.[124,125] Meanwhile, the layered/spinel heterointerface serves as a fast transport junction, which helps maintain Na^+ migration pathways even when the layered lattice undergoes stress accumulation or local distortion.[126,127]

To construct the layered/spinel composite configuration, the electrochemical Li^+/Na^+ exchange is frequently used; here, the spinel $LiMn_2O_4$ (LMO-S) is generally employed as the precursor. Li^+ ions are initially extracted from LMO-S upon charging to 4.3 V (*vs.* Li/Li^+), followed by Na^+ insertion into the delithiated spinel structure upon discharging to 2.0 V (*vs.* Na/Na^+). Upon Na^+ insertion, the rearrangement of Mn^{3+} and Mn^{4+} induces a partial structural transformation from the spinel to a layered structure, resulting in the formation of a spinel/layered Mn-based composite (NaMO-SL) (Fig. 6a).[104] In NaMO-SL, the layered phase underwent a reversible O3 → P3 → P″3 transformation during cycling (Fig. 6b and c). The (111) diffraction peak of the spinel phase shifted slightly to higher angles only when the voltage exceeded 3.3 V, indicating that the spinel phase participated in Na^+ extraction at high potential and maintained structural stability. The reversible Mn^{4+}/Mn^{3+} redox reaction indicates the excellent stability of NaMO-SL during cycling (Fig. 6d and e). Overall, this electrochemically derived

spinel-layered intergrowth configuration allows the layered domains to deliver high capacity, while the spinel phase alleviates lattice strain and mitigates the O3 → P3 → P″3 transitions, thereby effectively suppressing phase-transition-driven degradation in Mn-based layered cathodes.

Spinel-assisted local interlocking can pin the layered framework and stabilize TM chemistry, offering an effective route to stabilize layered oxides under wide voltage windows and prolonged cycling. For example, to address the irreversible P3 → O3′ phase transition and the concomitant Mn dissolution in P3-type layered cathode materials, Li *et al.* proposed an interfacial spinel local interlocking strategy.[99] By regulating the calcination temperature, a spinel phase was induced at the grain boundaries, enabling its interlocking with the P3 layered phase to form $Na_{0.5}Mg_{0.2}Co_{0.15}Mn_{0.65}O_2$ (NaMCM-700) (Fig. 6f). Mechanistically, the spinel domains function as rigid structural anchors that locally pin the layered framework, thereby suppressing TM-layer gliding and alleviating Jahn–Teller distortion during Na^+ extraction. As revealed by *in situ* X-ray diffraction (XRD), NaMCM-700 undergoes a reversible multiphase evolution (P3/spinel ↔ P3/spinel + O3′), rather than transforming fully and irreversibly into O3′ (Fig. 6g and h). Meanwhile, Mn K-edge X-ray absorption spectroscopy (XAS) (Fig. 6i and j) and depth-profile X-ray photoelectron spectroscopy (Fig. 6k) provide evidence for a more homogeneous Mn distribution, indicating effective suppression of Mn dissolution/migration and highlighting the coupled stabilization of structural and chemical integrity. Benefiting from this interfacial spinel interlocking effect, the P3/spinel electrode delivers substantially improved cycling stability, retaining 65% of its capacity after 100 cycles at 0.1C, far outperforming the pristine P3 counterpart, which retains 41%.

Apart from the layered/spinel biphasic structures, the multiphasic configurations like P2/P3/spinel are also common strategies to ameliorate the properties of layered cathodes. Hou *et al.* prepared a three-phase-coexisting $Na_{0.5}(Ni_{0.2}Co_{0.15}Mn_{0.65})O_2$ (LS-NCM) nanocomposite based on the complementary characteristics of P3, P2, and spinel phases.[128] As shown in Fig. 7a–d, the (311) diffraction peak of the spinel phase shifted to higher angles during discharge, indicating electrochemical activity of the $Fd\bar{3}m$ spinel phase, which corresponds to Na^+ insertion. Meanwhile, the 3D Na^+ diffusion pathways in the spinel structure improve Na^+ transport kinetics in this hybrid cathode during redox reactions. At the end of the charge process, the unit cell shrank along the *c*-axis (Fig. 7c), while in the following discharge process, it further decreased and then increased, finally recovering to the initial state. These results demonstrate the structural stability of this P3/P2/spinel intergrowth composite. Consistently, LS-NCM maintains 60% of its 0.1C capacity even at 10C (Figure 7e and f), and exhibits superior long-term capacity retention over 400 cycles at 1C (Fig. 7g), benefiting from the spinel phase that enables fast Na^+ transport kinetics. Furthermore, the LS-NCM ‖ hard-carbon full cell (Fig. 7h and i) delivers a capacity of ~100 mAh g^{-1} at 0.1C with nearly 100% initial coulombic efficiency and an average voltage of ~3.0 V, while maintaining 90.6% capacity retention after 400 cycles at 0.5C. Overall, the layered/spinel multiphasic
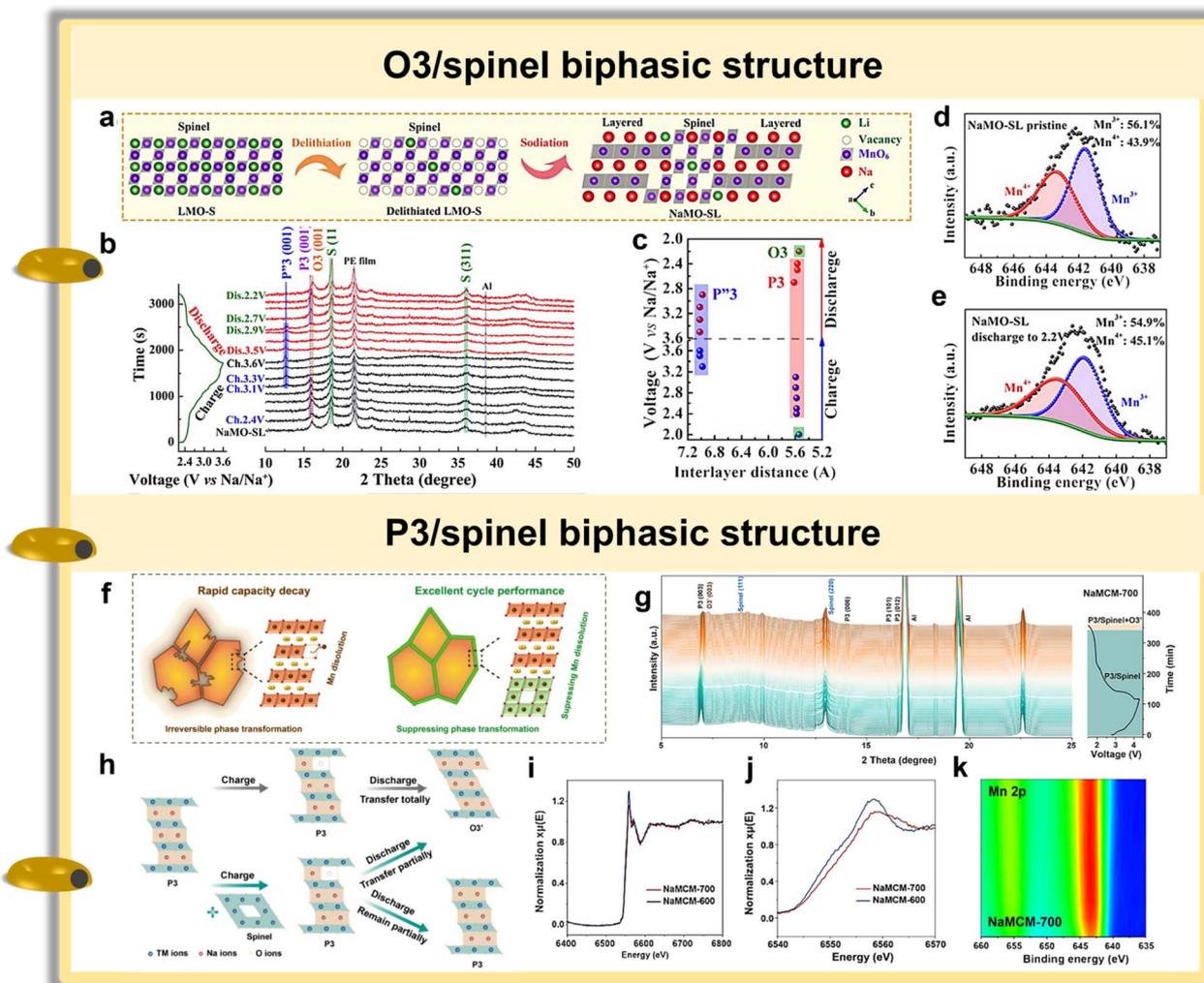
Fig. 6 (a) The schematic illustration of electrochemical Li$^+$/Na$^+$ exchange. (b) *Ex situ* XRD patterns of NaMO-SL during the charge/discharge process. (c) The interlayer distances of the layered component at various voltages. The XPS Mn 2p spectra of NaMO-SL in the (d) pristine and (e) discharged to 2.2 V states. Reproduced with permission.[104] Copyright 2020, American Chemical Society. (f) Schematic diagram of the interfacial spinel interlocking strategy. (g) *In situ* synchrotron-based XRD patterns of NaMCM-700 collected during the first charge/discharge within 1.5–4.3 V. (h) Diagrammatic representation of the structural evolution during Na$^+$ extraction/insertion. (i and j) Mn XAS spectra of NaMCM-600 and NaMCM-700 after 100 cycles. (k) XPS depth-profile spectra of Mn in NaMCM-700. Reproduced with permission.[99] Copyright 2024, American Chemical Society.

intergrowth architecture can maintain a stable phase constitution during (de)sodiation and enable reversible lattice evolution, which underpins the simultaneously achieved high-rate capability, prolonged cycling stability, and full-cell-level feasibility of layered Na$_x$TMO$_2$ cathodes.

In most cases, elemental composition regulation is a frequently used strategy to construct layered/spinel coexisting configurations. For instance, Zhu *et al.* designed a P2@P3 integrated-spinel cathode Na$_{0.5}$Ni$_{0.1}$Co$_{0.15}$Mn$_{0.65}$Mg$_{0.1}$O$_2$ (LLS-NaNCMM) (Fig. 7j) by regulating the Mg content.[121] Benefiting from the high electronic conductivity of the integrated-spinel phase (10^{-3}–10^{-4} S cm^{-1}), LLS-NaNCMM exhibited an accelerated rate capability (97.5 mAh g^{-1} at 5C) (Fig. 7k). Due to Mg substitution, the complex phase transformations of P2/P3/spinel → P2/P3″/spinel → P2/P3/spinel → P2′/P3″/spinel are

successfully restrained and simplified to P2/P3/spinel → P2/P3″/spinel (Fig. 7l). The Mn K-edge X-ray absorption near edge structure (XANES) spectra of LLS-NaNCMM (Fig. 7m and n) showed no noticeable separation or abrupt change in intensity, indicating that Mg doping didn't alter the octahedral coordination environment of Mn and effectively mitigated the Jahn–Teller distortion associated with Mn^{3+}. As shown in Fig. 7o, the LLS-NaNCMM cathode delivers a satisfactory capacity retention of 80.6% after 200 cycles at 2C, while maintaining a high and stable coulombic efficiency.

Similarly, Chou's group reported a strain engineering strategy *via* local chemistry manipulation and designed a P2/P3/spinel tri-phase heterostructure Na$_{0.5}$Ni$_{0.05}$Co$_{0.15}$Mn$_{0.65}$Mg$_{0.15}$O$_2$ (LLS-NaNCMM15), where Mg substitution facilitates the stabilization of the spinel phase and simplifies the multiphase
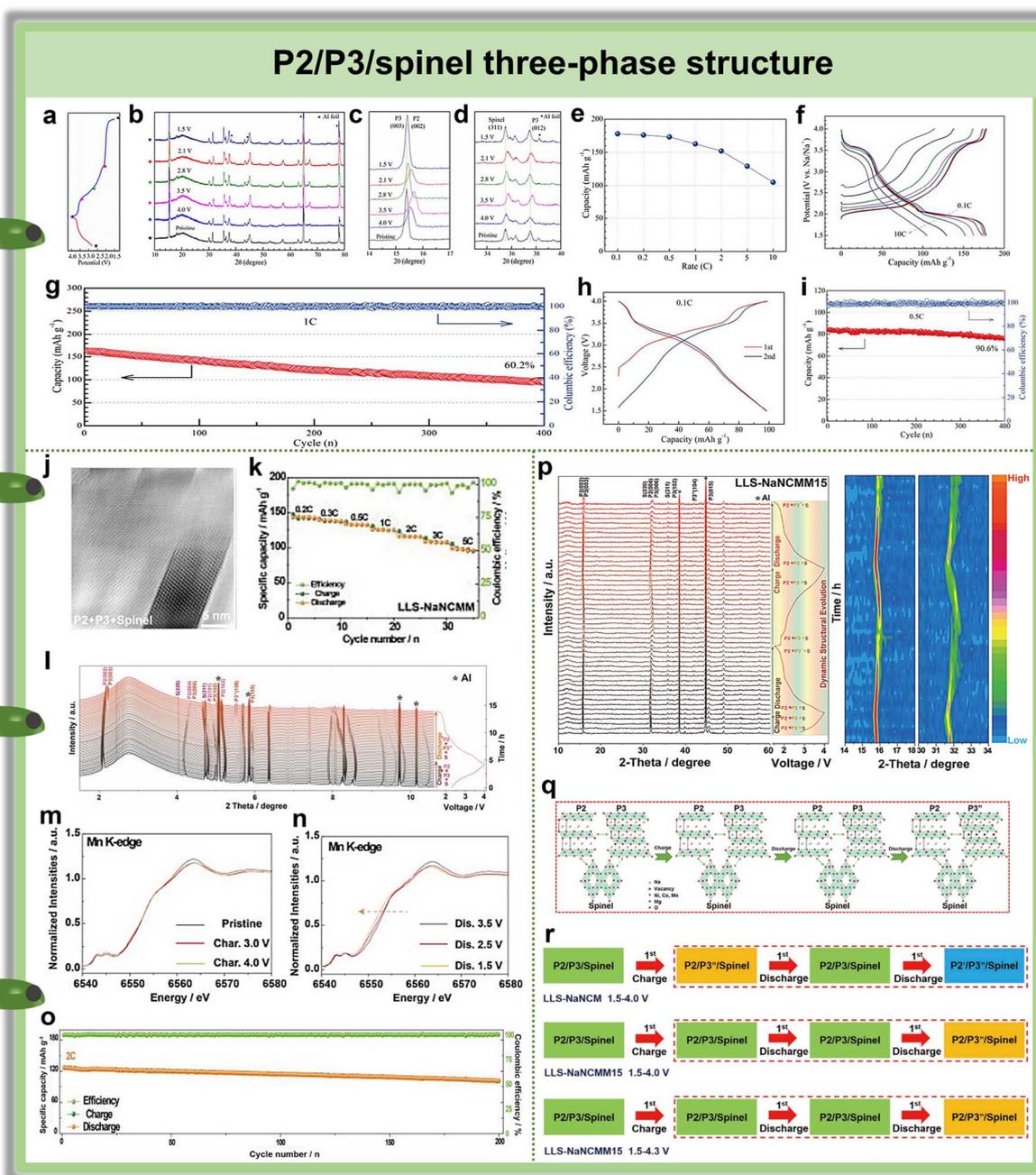
Fig. 7 (a–d) *Ex situ* XRD patterns collected during the initial charge/discharge process of LS-NCM within 1.5–4.0 V (*vs.* Na/Na⁺). (e) Reversible capacity and (f) corresponding charge/discharge curves of the LS-NCM from 0.1C to 10C. (g) Long-term cycling stability of LS-NCM. The discharge/charge curves at 0.1C (h) and cycling stability (i) of the LS-NCM ‖ 1 M NaClO₄ EC/DEC ‖ hard carbon full cell. Reproduced with permission.[128] Copyright 2018, American Chemical Society. (j) HAADF-STEM and ABF-STEM images of LLS-NaNCMM. (k) Rate performance of LLS-NaNCMM. (l) *In situ* XRD patterns collected during the first cycle at 0.1C and the corresponding charge/discharge curves. *Ex situ* XANES spectra at the Mn K-edge of LLS-NaNCMM collected at different (m) charge and (n) discharge states. (o) Cycling performance of LLS-NaNCMM over 200 cycles at 2C. Reproduced with permission.[121] Copyright 2020, Wiley-VCH. (p) *In situ* XRD patterns of LLS-NaNCMM15. (q) Schematic illustration of the crystal structural evolution of LLS-NaNCMM15 during cycling. (r) Schematic representations of crystal structural evolution for the cathodes within different voltage ranges. Reproduced with permission.[129] Copyright 2022, Wiley-VCH.

evolution. As revealed by *in situ* XRD, during Na⁺ extraction/insertion within 1.5–4.0 V, the P2 (002)/(004) and P3 (003)/(006) reflections shift reversibly without generating extra peaks, while the P3 → P3″ transition is identified by the disappearance of the P3 (015) peak and the emergence of the

P3″ (104) peak (Fig. 7p). Importantly, compared with the Mg-free counterpart, the reduced peak shifts indicate that Mg substitution is used to mitigate the structural instability associated with multiphase evolution. These smaller peak shifts indicate reduced volume change and lattice strain, meaning the
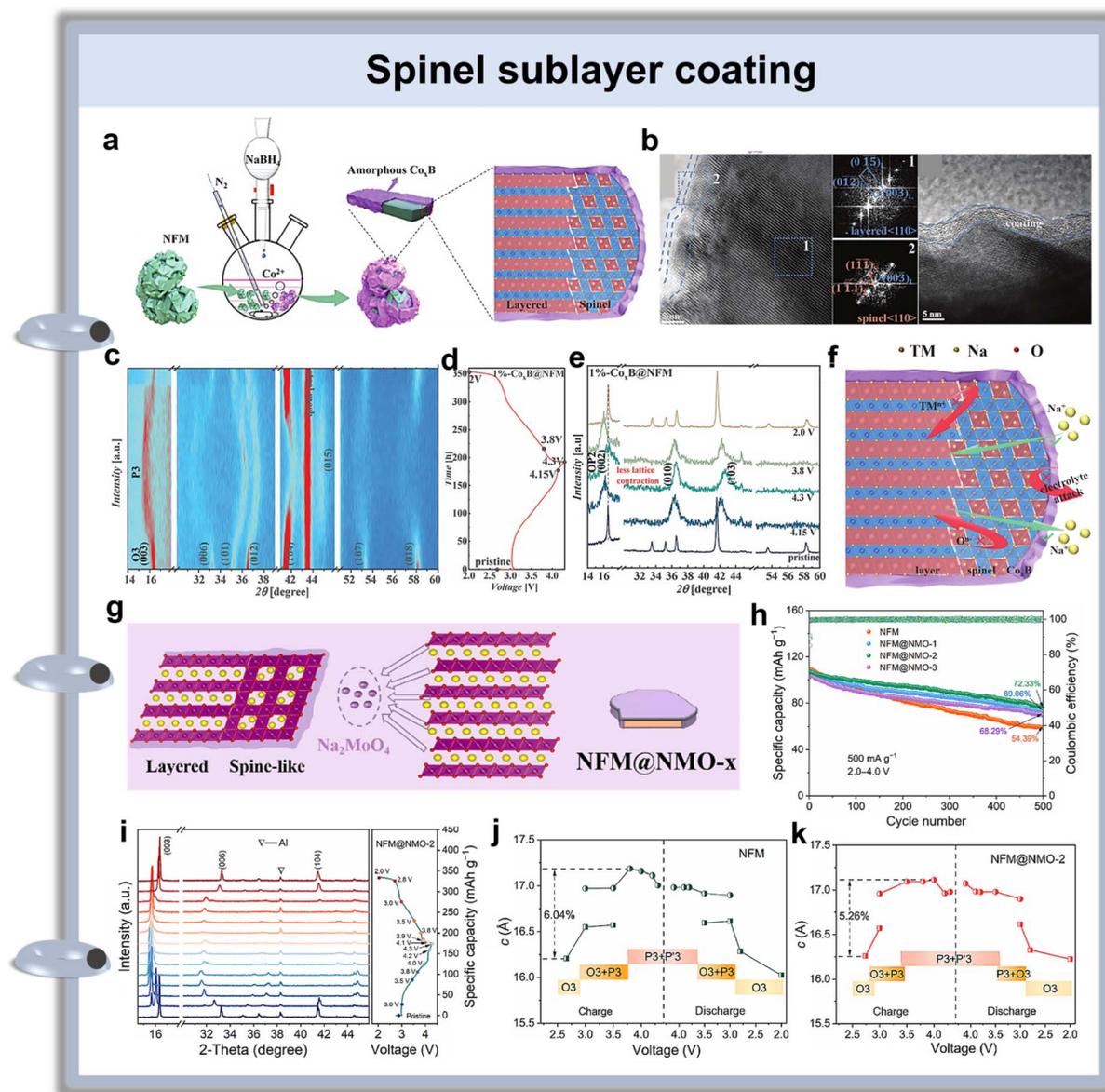
Fig. 8 (a) Schematic diagram for the synthesis process of 1wt%-Co$_x$B@NFM. (b) HRTEM images and corresponding FFT of 1wt%-Co$_x$B@NFM. *In situ* XRD patterns (c) and corresponding charge−discharge profiles (d) as well as *ex situ* XRD patterns at different charge states (e) for 1wt%-Co$_x$B@NFM. (f) Structural model for the surface of 1wt%-Co$_x$B@NFM. Reproduced with permission.[109] Copyright 2024, Wiley-VCH. (g) Schematic diagram of the crystal configuration of NaNi$_{1/3}$Fe$_{1/3}$Mn$_{1/3}$O$_2$@NMO-*x*. (h) Electrochemical performance of NaNi$_{1/3}$Fe$_{1/3}$Mn$_{1/3}$O$_2$ and NaNi$_{1/3}$-Fe$_{1/3}$Mn$_{1/3}$O$_2$@NMO-*x* in the voltage window of 2.0−4.0 V. (i) *Ex situ* XRD patterns of NFM@NMO-2 in the first cycle. Calculated lattice parameter along *c*-axis of (j) NaNi$_{1/3}$Fe$_{1/3}$Mn$_{1/3}$O$_2$ and (k) NFM@NMO-2 in different charge/discharge states. Reproduced with permission.[123] Copyright 2025, Elsevier.

spinel component contributes to overall lattice stabilization. Accordingly, the schematic in Fig. 7q summarizes a simplified and reversible phase evolution (P2/P3/spinel → P2/P3″/spinel) with only minor volume change and lattice strain. To further highlight the stress/strain-regulation effect under more demanding conditions, Fig. 7r schematically contrasts the phase-transition pathways of cathodes at different cut-off voltages. At an upper cut-off of 4.3 V, the Mg-substituted LLS-NaNCMM15 still undergoes a simple P2/P3/spinel → P2/P3″/spinel transition. Meanwhile, the spinel phase maintains its

structure during cycling and thus contributes to structural stabilization.[129]

3.1.2 Spinel sublayer coating. The spinel coating often involves the construction of a spinel-rich interphase, followed by an outer protective coating.[130,131] In this dual-layer configuration, the inner spinel layer stabilizes the near-surface lattice and suppresses surface reconstruction, while the outer coating primarily blocks parasitic reactions (*e.g.*, electrolyte attack and surface oxygen loss), thereby producing a more stable cathode-electrolyte interphase (CEI) and preserving the bulk layered framework.[132,133]

The spinel structure possesses superior stability and open 3D Na$^+$ transport pathways. *In situ* surface reconstruction by coating the layered phase with a spinel-like lattice not only enhances surface Na$^+$ transport kinetics but also stabilizes the bulk layered structure. Feng *et al.* constructed a dual conformal protective layer on the surface of NaNi$_{0.33}$Fe$_{0.33}$Mn$_{0.34}$O$_2$ through liquid-phase reduction (Fig. 8a), yielding NaNi$_{0.33}$-Fe$_{0.33}$Mn$_{0.34}$O$_2$@Co$_x$B (1wt%-Co$_x$B@NFM),[109] as evidenced by high resolution transmission electron microscope (HRTEM) and fast fourier transform (FFT) analyses, which reveal a three-section surface configuration comprising amorphous Co$_x$B, spinel, and layered regions (Fig. 8b). *In situ* XRD 2D contour mapping collected between 2.0 and 4.0 V at 0.2C (Fig. 8c) reveals a reversible O3 → P3 evolution for 1 wt% Co$_x$B@NFM, where the characteristic reflections shift continuously during charge and return upon discharge. *Ex situ* XRD results reveal that the 1 wt% Co$_x$B@NFM begins to transform into an OP2 structure when charged to 4.15 V with the appearance of (002), (010), and (103) peaks. As charging continues to 4.3 V, the (002) peak consistently moves to higher angles, indicating a contraction of the lattice parameter *c* (Fig. 8d and e). Notably, compared with pristine NaNi$_{0.33}$Fe$_{0.33}$Mn$_{0.34}$O$_2$, the smaller high-angle deviation indicates reduced lattice contraction. This can be ascribed to a coherent lattice-matched surface spinel layer that serves as a pillar/anchor to inhibit lattice distortion and slab sliding, along with an outer amorphous Co$_x$B overlayer that suppresses interfacial parasitic reactions and configuration collapse (Fig. 8f). This allows 1wt%-Co$_x$B@NFM to maintain an intact structure during prolonged cycling, enhancing phase-transition reversibility and cycling stability. Accordingly, after 300 cycles, 1wt%-Co$_x$B@NFM retains a capacity retention of 79.6%, significantly outperforming the 51.4% retention of NaNi$_{0.33}$Fe$_{0.33}$Mn$_{0.34}$O$_2$.

Obtained by introducing 2 wt% (NH$_4$)$_6$Mo$_7$O$_{24}$·4H$_2$O (NMO) precursor and featuring a heterogeneous Na$_2$MoO$_4$/spinel/O3 triple-layer structure (Fig. 8g), the NFM@NMO-2 exhibits significant improvements in cycling stability and rate performance compared with unmodified NaNi$_{1/3}$Fe$_{1/3}$Mn$_{1/3}$O$_2$. It delivers superior long-term cycling at 500 mA g^{-1}, retaining 72.33% capacity after 500 cycles (*vs.* 54.39% for NaNi$_{1/3}$Fe$_{1/3}$-Mn$_{1/3}$O$_2$) (Fig. 8h).[123] Herein, the Mo^{6+} with a high valence state and strong Mo–O bonds in the O3 phase enlarges the TM-layer spacing and enhances structural stability.[134,135] The diffraction peaks of NFM@NMO-2 exhibit higher symmetry during cycling than those of NaNi$_{1/3}$Fe$_{1/3}$Mn$_{1/3}$O$_2$, suggesting improved structural reversibility (Fig. 8i). With Na$^+$ extraction and the introduction of high-valent Mo^{6+}, Mn in the near-surface region may undergo reduction, resulting in a layered-to-spinel phase transformation. The as-formed nanoscale spinel layer can mechanically constrain the internal layered structure, thereby limiting volume change during charge–discharge processes (Fig. 8j and k). Furthermore, XPS analysis of the CEI layers on NFM@NMO-2 and the pristine material revealed that the intensities of C=O and O=C–O species on the NFM@NMO-2 cathode were significantly weaker, indicating that the spinel-containing surface can suppress the formation of organic-rich decomposition products. This surface-to-bulk synergistic

modification strategy offers an efficient and scalable approach for developing high-performance Na$_x$TMO$_2$ for SIBs.

3.1.3 Lattice-stress regulation. The introduction of the spinel phase can homogenize the stress distribution, reduce stress concentration, and thus inhibit microcrack initiation and propagation. This mechanical stabilization is tightly coupled with kinetics: fewer cracks and a more intact interface generally translate to lower impedance growth and more sustained Na$^+$ transport over long-term cycling.

Upon desodiation, substantial stress is generated in the non-stoichiometric lattice due to electrostatic repulsion between adjacent O layers, which generally leads to interlayer sliding, TM-ion migration, and structural collapse. To reduce the lattice stress in layered oxides during cycling, the layered/spinel-type Na$_{0.44}$Mn$_{0.8}$Mg$_{0.2}$O$_2$ (LS-NaMM20) was prepared by substituting Mn sites in tunnel-type Na$_{0.44}$MnO$_2$ with Mg.[136] As seen from the COMSOL simulations (Fig. 9a), the von Mises stress in this layered/spinel system was significantly lower than that in the pure layered and layered/tunnel structures. The tight interfacial contact enabled uniform stress transfer, preventing layer sliding caused by localized stress concentration. *In situ* XRD (Fig. 9b) captured the reversible P2 ↔ P2′ phase transition in this layered/spinel heterostructure during charge and discharge, which is ascribed to the fact that the 3D rigid framework of the spinel phase effectively reinforces the TM layer, suppressing irreversible phase transitions. The reversible Mn^{3+}/Mn^{4+} redox reaction, with a highly synchronized valence state change with the structural evolution, corroborated stress relaxation (Fig. 9c and d). Collectively, these results demonstrate that spinel-enabled stress homogenization is a key mechanism for stabilizing layered cathodes during repeated (de)sodiation.

In the P2/spinel coherent heterostructure Na$_{0.65}$Mn$_{0.67}$Co$_{0.17}$Ni$_{0.17}$B$_{0.05}$O$_{2+y}$ (NaMCNB) constructed through a boric-acid molten-salt treatment, the characteristic peaks of the P2 phase exhibited slight reversible shifts, and no OP4 phase diffraction peak appeared, confirming that the spinel layer effectively suppressed detrimental phase transitions (Fig. 9e and f).[122] Based on the HAADF-STEM and geometric phase analysis (GPA) images obtained after 100 cycles, the surface of NaMCNB remains free of discernible cracks and exhibits a relatively homogeneous internal strain distribution. This can be attributed to the fact that, during cycling, the lattice contraction of the spinel-like phase complemented the lattice expansion of the layered phase, effectively offsetting the volume change and preventing non-uniform stress accumulation and the associated intragranular crack formation (Fig. 9g–i). The essence of this phenomenon is that the spinel-like structure along the [011] zone axis possesses oxygen-sublattice arrangements similar to those of the P2-type structure along the [010] direction, which ensures compatibility in oxygen stacking and enables good lattice matching between the spinel-like layer and the P2 phase. The coherent interface thus formed allows the spinel-like nanolayer to act as a "locking layer" (Fig. 9j), which effectively prevents the gliding of TMO$_6$ slabs in the P2 phase during Na$^+$ extraction.
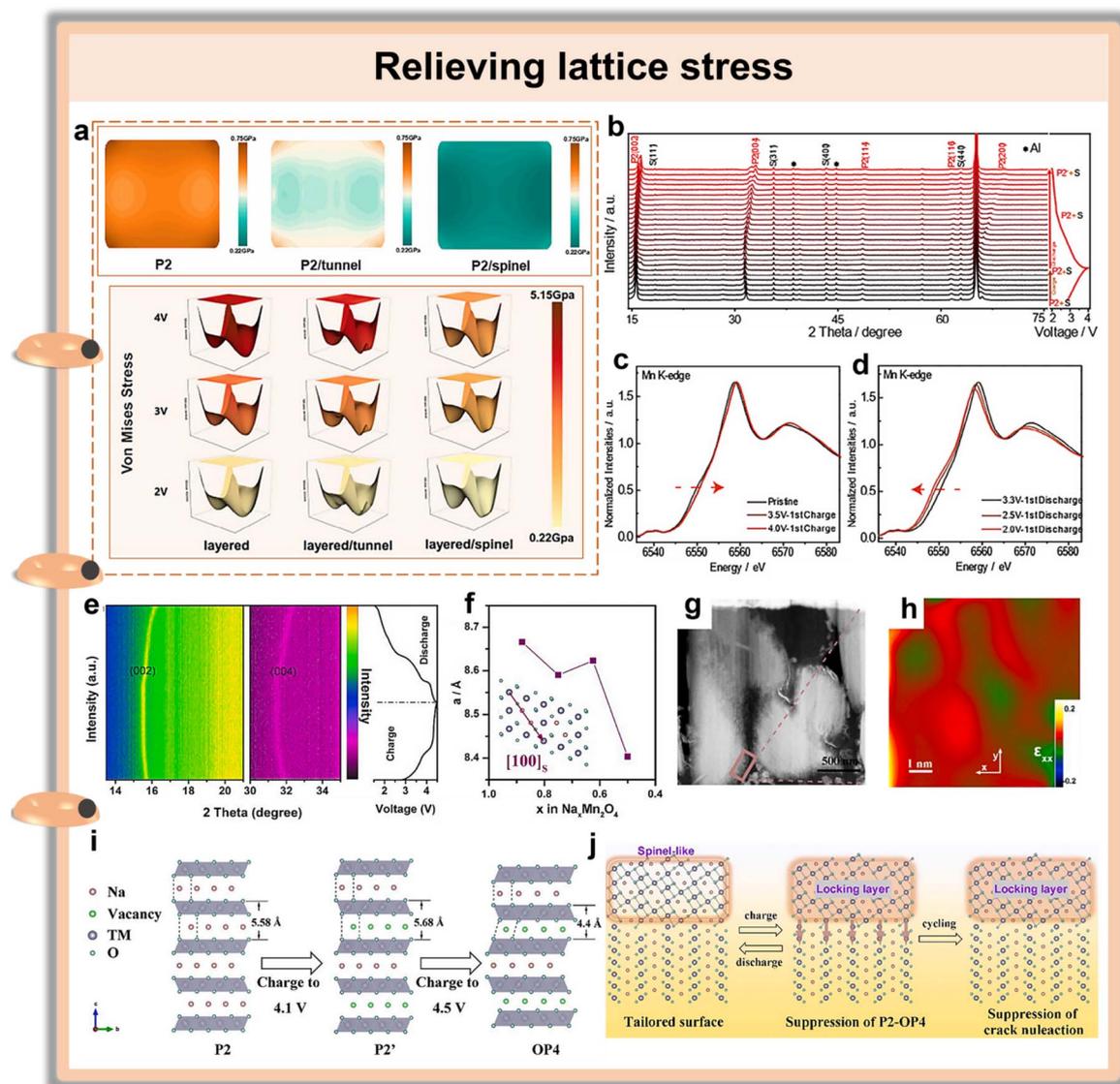
Fig. 9 (a) The von Mises stress of layered, layered/tunnel, and layered/spinel structures at different charge states. (b) *In situ* XRD pattern of the LS-NaMM20 in the first cycle. (c and d) *Ex situ* XANES spectra at the Mn K-edge of LS-NaMM20 collected at different charge−discharge states. Reproduced with permission.[136] Copyright 2025, Wiley-VCH. (e) Contour plots of the (002) and (004) peaks for NaMCNB. (f) The lattice constant changes for spinel-$Na_xMn_2O_4$ calculated using first principles. (g and h) HAADF-STEM images and corresponding GPA patterns of NaMCNB after 100 cycles between 1.5 and 4.5 V. (i) Crystal models illustrating the structural transitions in the B-free $Na_{0.65}Mn_{0.67}Co_{0.17}Ni_{0.17}O_{2+y}$. (j) Structural evolution near the surface of NaMCNB. Reproduced with permission.[122] Copyright 2020, Elsevier.

3.2 Enhancing air stability

As mentioned above, the P2- and O3-type Na_xTMO_2 can spontaneously react with moisture and CO_2 in the air, which consume active Na^+ and produces detrimental by-products, thereby significantly diminishing capacity and rate capability. To address this issue, constructing a spinel coating layer on the surface of layered-phase particles provides a robust protective barrier for the bulk material (Fig. 10). Specifically, the spinel coating effectively reduces the diffusion of H_2O and CO_2 from the air into the layered host material, suppressing Na^+/H^+ exchange and the formation of $Na_2CO_3/NaHCO_3$.[137–139] The spinel layer also helps suppress TM ion dissolution and mitigate air-induced structural degradation, dramatically

enhancing the air stability of the layered cathode materials (Fig. 10).

Although the P2-type Fe/Mn-based layered oxide cathodes have attracted tremendous interest because of their cost effectiveness, environmental friendliness, and diverse valence states, air sensitivity remains their severe drawback. In 2025, Wang *et al.* synthesized a P2-$Na_{0.67}Fe_{0.3}Mn_{0.7}O_2$ cathode with a spinel $MnFe_2O_4$ coating layer and bulk OVs ($NFM(OV) + MnFe_2O_4$).[140] The characteristic diffraction peaks of $NFM(OV) + MnFe_2O_4$ showed no obvious change after being placed in air for one month or even immersed in water for 3 h, whereas the unmodified sample rapidly developed new diffraction peaks assigned to hydrated phases and $NaHCO_3$ (Fig. 11a). Moreover, after cycling, the spinel layer exhibited minimal and uniform
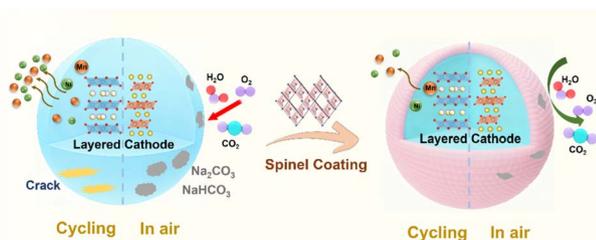
Fig. 10 Schematic illustration of enhanced air stability for layered oxides enabled by integrating spinel phase.

internal strain and, notably, facilitated the formation of a thinner and more uniform CEI layer compared to the thick and irregular CEI on the pristine electrode (Fig. 11b). These observations confirm that the spinel coating layer effectively blocked electrolyte decomposition and by-product accumulation. In this configuration, the spinel coating layer acts as a physical barrier against air/electrolyte corrosion and provides open Na^+ diffusion pathways, while bulk OVs optimize ion migration and redox activity (Fig. 11c). Benefiting from this dual-regulation strategy, NFM(OV) + $MnFe_2O_4$ delivered a discharge capacity of 185.7 mAh g^{-1} at 0.1C and a capacity retention of 82.6% after 300 cycles at 2C. Overall, the $MnFe_2O_4$ spinel shell is not just an electrochemically active coating, but an environmentally robust barrier that fundamentally mitigates the air- and moisture-sensitivity of Fe/Mn-based layered oxides.

Strategies for enhancing the air stability of O3-type layered oxide materials primarily focus on two approaches: element doping and surface coating. Element doping can inhibit the intrusion of H_2O and CO_2 by strengthening Na–O bonds, but it may further increase the Na^+ diffusion energy barrier.[141,142] Although traditional surface coatings (Al_2O_3, TiO_2, *etc.*) can enhance air stability, they often impede Na^+ diffusion and result in decreased capacity.[143,144] To address this issue, Li *et al.* constructed a spinel@O3-type layered composite, $Na_{0.9}Mn_{0.5}Ni_{0.5}Cu_{0.1}O_{2+x}$ (NMNCO-SL), by coating a Cu-rich spinel phase onto the surface of $Na_{0.9}Mn_{0.5}Ni_{0.5}O_2$ (NMNO). Benefiting from the spinel's unique 3D ion-transport channels and intrinsic air stability, the NMNCO-SL exhibited significantly enhanced air stability without sacrificing ion-transport kinetics.[145] Under the same conditions (65% humidity, 30 °C), NMNO exhibited a noticeable $Na_2CO_3·xH_2O$ phase after 10 h of exposure. Na^+ loss and alkaline substances such as NaOH and Na_2CO_3 on the surface triggered the defluorination reaction of polyvinylidene fluoride (PVDF) binder, which reduced the mechanical properties of the electrode (Fig. 11d). The surface spinel phase on the NMNCO-SL acts as a protective layer, effectively preventing the penetration of H_2O and CO_2 from air into the interlayers. Besides, the Cu-rich spinel phase surface can alleviate interlayer slipping caused by Na^+ deintercalation and suppress excessive expansion along the *c*-axis (Fig. 11e). Therefore, this material retains 70% of its initial capacity after 1000 cycles at 5C, which is markedly superior to that of NMNO (47.7%), demonstrating the potential prospects of spinel coating engineering. For the biphasic systems like P2/P3-type cathode materials, the surface lattice-matched engineering achieved through *in situ* spinel

interfacial reconstruction can effectively isolate the layered phases from environmental H_2O/CO_2 as well, thereby greatly enhancing air stability. For the spinel-coated P2/P3 hetero-structure $Na_{0.5}Mg_{0.2}Co_{0.15}Mn_{0.65}O_2$ (P2/P3@spinel-NaMCM) synthesized at 800 °C (Fig. 11f),[107] the spinel layer, which serves as a dense hydrophobic barrier, effectively prevents moisture intrusion. The XRD patterns of P2/P3@spinel-NaMCM remain almost unchanged after air exposure (Fig. 11g), and a large water contact angle of approximately 100.86° is observed (Fig. 11h). The tailored spinel-coated structure remains intact after exposure to humid air at 50% relative humidity for 7 days, providing an effective solution to the air-sensitivity issue faced by multiphase layered oxides. Notably, the intrinsic hydrophobicity of the spinel surface also plays a critical role during electrochemical cycling by tolerating trace amounts of water in the electrolyte.[146,147] Generally, water in the electrolyte induces the hydrolysis of PF_6^- salts,[148,149] generating HF that corrodes the cathode surface and accelerates transition metal dissolution.[150] The spinel layer can therefore serve as a physical barrier against HF attack, further stabilizing the layered structure under operating conditions.

In 2017, Guo *et al.* constructed a Ti-rich spinel-type $NaMn_{0.8}Ti_{0.1}Ni_{0.1}O_2$ (NMTN) based on P2/O3-type $NaMnO_2$.[105] As illustrated in the schematic diagrams (Fig. 11i), the unmodified $NaMnO_2$ was susceptible to reacting with electrolyte and H_2O/CO_2 in air, which triggered Mn^{3+} disproportionation and Mn^{2+} dissolution. In contrast, the Ti^{3+}-enriched spinel-like shell acted as a physical barrier to constrain structural collapse. After exposure to humid air for 3 days, the unmodified $NaMnO_2$ showed a new hydrated birnessite peak at around 12°, whereas the NMTN retained the original layered diffraction peaks (Fig. 11j and k), clearly highlighting the crucial role of the spinel-like interface in enhancing the air stability of P2/O3 layered cathodes. Mechanistically, this exceptional air stability originates from the inherently stable crystal structure of the spinel-like interface, which effectively blocks H_2O molecules. Simultaneously, this protective layer physically isolates the chemically active Mn^{3+} from electrolyte attack, mitigating side reactions such as the disproportionation of Mn^{3+} and Mn dissolution, whereas the pristine counterpart showed substantial Mn deposition accompanied by a significant increase in interfacial resistance (Fig. 11l).

In summary, across different layered frameworks, spinel-related surface engineering consistently enhances air stability, although the dominant contribution is phase-dependent. For the single phase Na_xTMO_2 like P2 and O3-type structures, the spinel coating serves as a physical barrier against electrolyte attack, suppresses lattice-oxygen release and interfacial side reactions, and facilitates rapid Na^+ kinetics. Apart from that, the spinel phase can inhibit H_2O/CO_2 penetration and alleviate desodiation-induced interlayer gliding and *c*-axis over-expansion, effectively stabilizing the crystal structure during cycling. Notably, for the multiphase cathodes with P2/O3- or P2/P3-type configurations, the coupled phases synergistically combine complementary advantages, leading to enhanced electrochemical performance compared with their individual phases. Similarly, the spinel coating layer on the surface of
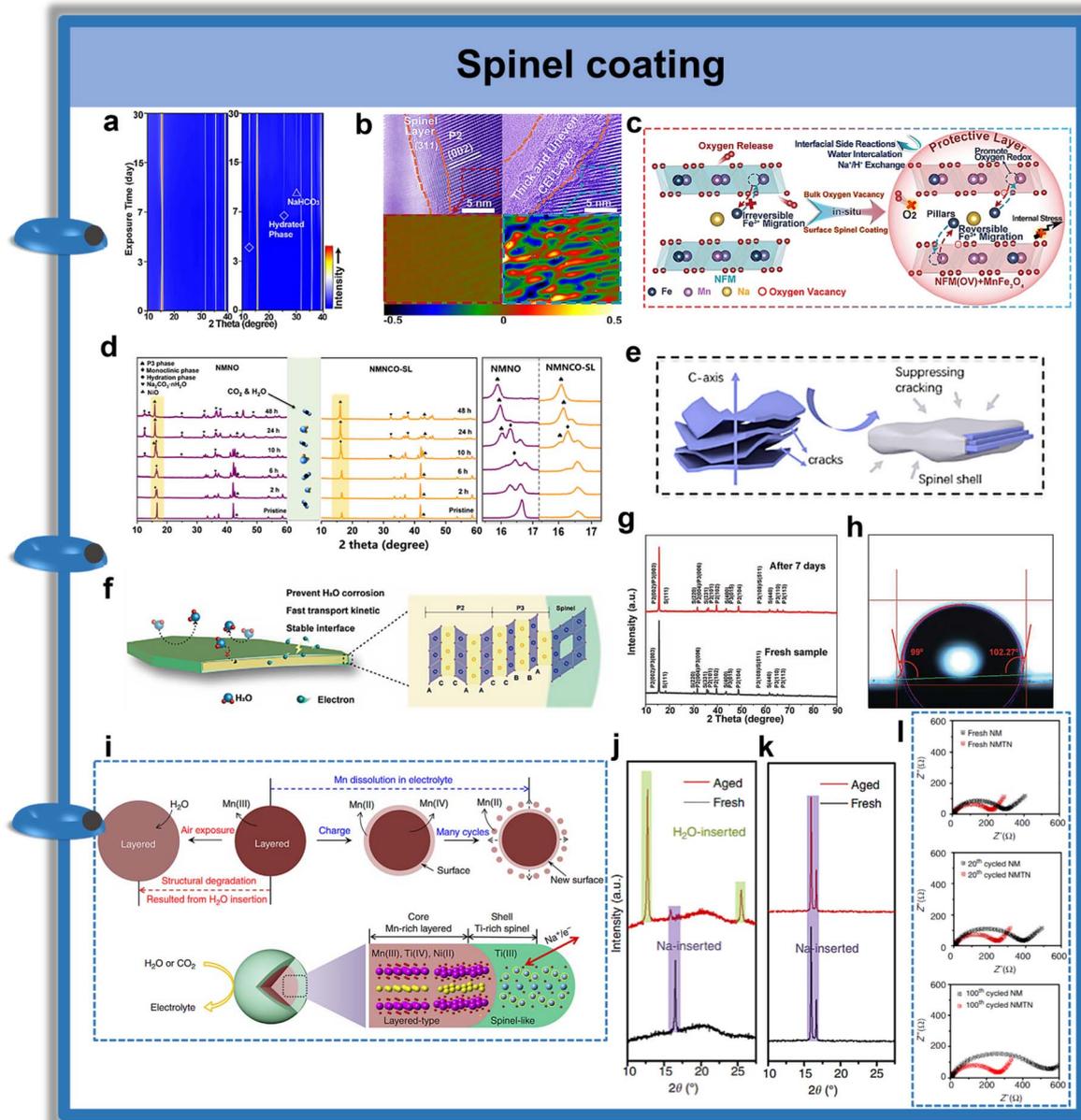
Fig. 11 (a) Contour maps of XRD patterns of NFM(OV) + $MnFe_2O_4$ (left) and $Na_{0.67}Fe_{0.3}Mn_{0.7}O_{1.965}$ (right) after being exposed to air for different times. (b) HRTEM images and corresponding GPA patterns of the NFM(OV) + $MnFe_2O_4$ (left) and $Na_{0.67}Fe_{0.3}Mn_{0.7}O_{1.965}$ (right) after 50 cycles. (c) Schematic illustration of bulk OVs and a surface spinel coating. Reproduced with permission.[140] Copyright 2025, Wiley-VCH. (d) The XRD patterns of pristine and aged NMNO and NMNCO-SL. (e) Schematic diagrams showing that the spinel shell suppresses structural changes. Reproduced with permission.[145] Copyright 2024, Elsevier. (f) Schematic representation of the crystal structure of P2/P3@spinel-NaMCM. (g) XRD patterns of fresh and exposed P2/P3@spinel-NaMCM. (h) The water contact angle of P2/P3@spinel-NaMCM. Reproduced with permission.[107] Copyright 2023, Wiley-VCH. (i) Enhancement mechanisms of $NaMnO_2$ by a NMTN coating. Structural changes of bare (j) and spinel-coated (k) $NaMnO_2$ after exposure to humid air for 3 days. (l) Impedance evolution of the $NaMnO_2$ and NMTN during cycling. Reproduced with permission.[105] Copyright 2017, Springer Nature.

multiphase configurations serves as an effective protection shell as well, further improving their properties.

3.3 Enhancing ion transport kinetics

Due to the larger ionic radius of Na^+ and the narrow interlayer spacing of Na_xTMO_2, the rate capability can't meet the demand for fast charging SIB devices.[151–154] Developing Na_xTMO_2 cathodes with high ion-transport kinetics has always been a key goal for

realizing their practical applications. Apart from enhancing phase and air stability, the spinel phase also provides a promising way to lower the Na^+ transport energy barrier in Na_xTMO_2 due to its open lattice framework. As shown in Fig. 12a, by introducing a Na_2MoS_4 spinel phase to connect the O3- and P2-type structures in $Na_{0.98}Ni_{0.3}Cu_{0.1}Ti_{0.05}Mo_{0.05}Mn_{0.5}O_2$ (NNMO), the

$Na_{0.98}Ni_{0.3}Cu_{0.1}Ti_{0.05}Mo_{0.05}Mn_{0.5}O_{2-\delta}S_\delta$ (NNMO-S) is formed. According to Born–Huang mechanical-stability

analysis, the bulk modulus of the spinel-type Na_2MoS_4 (29.197 GPa) is much lower than that of the O3 (147.362 GPa) and P2 (145.312 GPa) phases, which helps alleviate the internal stress and improves the structural strength (Fig. 12b).[98] Meanwhile, density functional theory (DFT) calculations showed that the Na^+ diffusion energy barrier in NNMO-S is lower than that of NNMO (Fig. 12c). This improvement is attributed to the introduction of a spinel phase, which induces *in situ* interfacial reconstruction and compresses the TM layer of the adjacent O3 phase along the *c*-axis. Consequently, the Na-layer channels expand, providing a more spacious transport path for Na^+ migration. This approach optimizes the Na^+ diffusion channels, enabling the material to operate at higher current densities. As shown in Fig. 12d, the O3/spinel/P2-type NNMO-S exhibits a higher Na^+ diffusion coefficient compared to the O3/P2-type NNMO. As expected, NNMO-S delivered a higher capacity retention of 62.34% than the NNMO (33.50%).

As aforementioned, embedding a spinel phase within the P2-type layered structure is an effective approach to construct P2/spinel composite cathodes, which can enhance electronic conductivity and capacity. To optimize the kinetic performance of the P2-type phase, Zheng *et al.* synthesized a P2/spinel-type $Na_{0.5}Ni_{1/6}Co_{1/6}Mn_{2/3}O_2$.[93] As revealed by HAADF-STEM characterization, the sample consists of intergrown P2 layered and spinel domains. The spinel phase exhibits oxygen-lattice arrangements very similar to those of the P2 phase, which, together with their structurally compatible cubic close-packed oxygen arrays, enables their successful integration. This highly compatible structure creates continuous channels for electron and Na^+ transport (Fig. 12e). Electrochemical impedance spectroscopy (EIS) was used to estimate the Na^+ diffusion coefficient by extracting the Warburg coefficient (σ_w) from the low-frequency Warburg region; the resulting D_{Na^+} for the P2/spinel composite was 1.22×10^{-10} cm^2 s^{-1}, about two orders of magnitude higher than that of the pure P2-type $Na_{0.67}Ni_{1/6}Co_{1/6}Mn_{2/3}O_2$ sample (8.30×10^{-13} cm^2 s^{-1}) (Fig. 12f and g).

Through lithium doping, Deng *et al.* constructed a layered-spinel coexisting structure $Na_{0.87}Li_{0.25}Ni_{0.4}Fe_{0.2}Mn_{0.4}O_{2+\delta}$ (LS-NFM) (Fig. 13a).[95] The LS-NFM maintained a capacity of 101 mAh g^{-1} even at a high current density of 120 mA g^{-1}, representing a 92% capacity retention compared with that at 12 mA g^{-1}, surpassing the undoped sample (Fig. 13b). The Na^+ diffusion coefficient of LS-NFM increased by an order of magnitude compared to that of the undoped sample
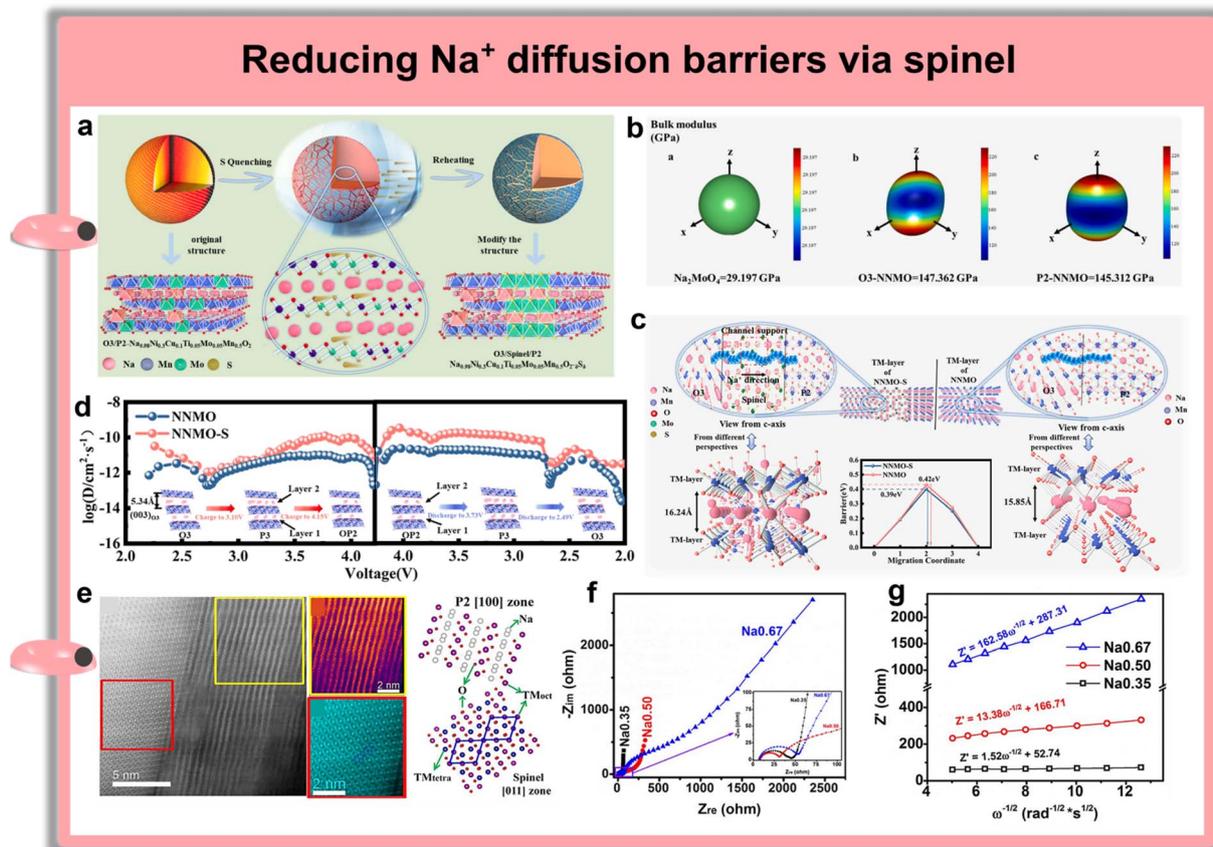

Fig. 12 (a) Schematic diagram of the preparation of NNMO-S. (b) Bulk modulus of each phase in NNMO-S. (c) Na^+ migration pathways and corresponding energy barriers in the samples. (d) D_{Na^+} of NNMO and NNMO-S in the first cycle. Reproduced with permission.[98] Copyright 2024, Elsevier. (e) HAADF-STEM images and schematic diagrams of the crystal configuration of $Na_{0.50}Ni_{1/6}Co_{1/6}Mn_{2/3}O_2$, and atomic models of the [100] zone-axis projection of the P2-type phase and the [011] zone-axis projection of the $Fd\overline{3}m$ spinel phase. (f) EIS plots of half-cells assembled with $Na_xNi_{1/6}Co_{1/6}Mn_{2/3}O_2$. (g) Relationship between real resistance and frequency, the slope (Warburg impedance coefficient) of which was used to calculate the Na^+ diffusion coefficient. Reproduced with permission.[93] Copyright 2016, The Electrochemical Society.
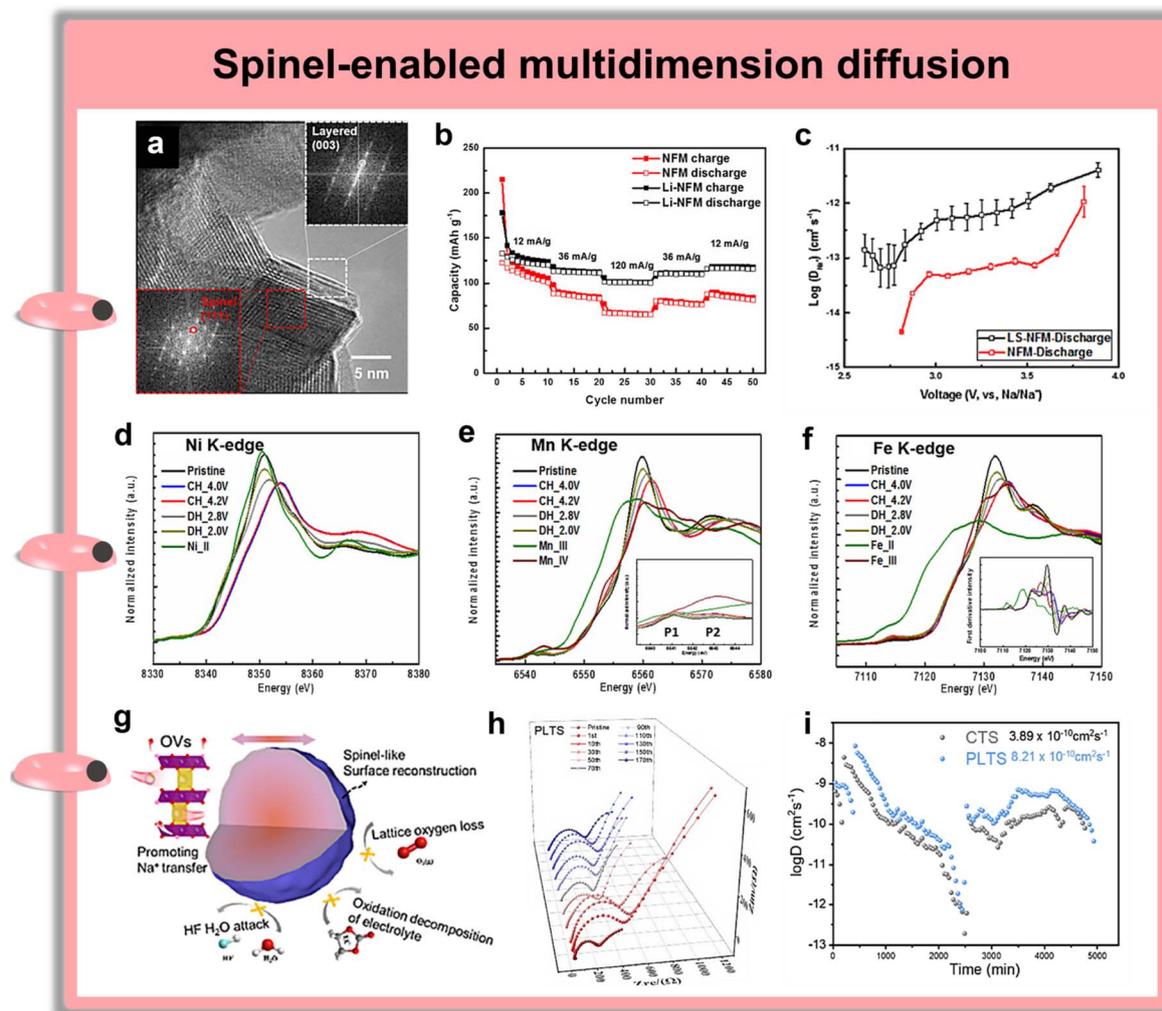
Fig. 13 (a) HRTEM images of LS–NFM. Rate capabilities (b) and GITT profiles (c) of LS–NFM and $NaNi_{0.4}Fe_{0.2}Mn_{0.4}O_2$. (d) Ni, (e) Mn, and (f) Fe K-edge XANES spectra of LS–NFM at different charge/discharge states. Reproduced with permission.[95] Copyright 2018, American Chemical Society. (g) Schematic illustrating the regulation of OVs and surface reconstruction via PLTS. (h) EIS plots of PLTS sample during prolonged cycling. (i) GITT profiles of CTS sample and PLTS sample. Reproduced with permission.[108] Copyright 2023, American Chemical Society.

$NaNi_{0.4}Fe_{0.2}Mn_{0.4}O_2$ (Fig. 13c). The improved Na$^+$ diffusivity is attributed to the 3D diffusion channels of the spinel structure, which provide direct connections between the layered and spinel components, greatly shortening the ion diffusion distance. Moreover, the Ni^{2+}/Ni^{4+} and Fe^{3+}/Fe^{4+} redox reactions in LS–NFM were highly reversible, while the bulk Mn remained predominantly in the +4 oxidation state (Fig. 13d–f). These results indicate that the spinel phase enhances cycling stability by stabilizing the local structure and redox reversibility of the layered host at high voltages, thereby suppressing irreversible structural evolution. This provides an effective strategy for optimizing O3-type Na$_x$TMO$_2$ cathodes.

In addition to the aforementioned methods, building a spinel phase by regulating surface OVs is also a valid approach. Chen et al. prepared P2-$Na_{0.72}Li_{0.24}Mn_{0.76}O_2$ via the PLTS method. The gradient-distributed surface OVs promote the formation of a robust spinel-like interfacial phase (Fig. 13g). During subsequent cycling, this spinel protective layer suppresses irreversible oxygen release and mitigates parasitic interfacial reactions.[108] As a result, compared with the conventional constant-temperature sintering (CTS) sample, the PLTS sample exhibits lower electrochemical impedance and a higher Na$^+$ diffusion coefficient (Fig. 13h and i).

4 Summary and prospects

In summary, we systematically review the synthesis methods for constructing layered/spinel symbiotic phases and systematically elucidate the mechanisms underpinning phase-transition suppression, air-stability improvement, and accelerated ion transport.[155–158] Fig. 14 presents a comparative analysis of specific capacities from representative studies. The data indicate that most heterostructures deliver higher reversible capacity than the original material. Despite its limited Na$^+$ storage capacity, the spinel's 3D diffusion channels couple with the layered phase's 2D channels to enhance Na$^+$ transport
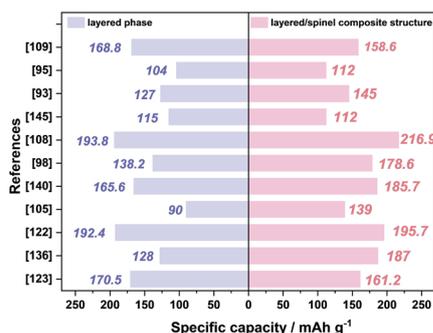
Fig. 14 Comparison of specific capacity between pure layered cathodes and layered/spinel composite heterostructures reported in the literature.

kinetics, enabling more complete utilization of the layered component's capacity.[95] However, a few studies indicate that the specific capacity of the heterostructure is actually lower than that of the original layered structure. This is because the introduction of TM elements with inert electrochemical activity, such as Cu[145] and Mo[123], reduces the relative content of highly active TM in the unit mass of material.[159–161] But in terms of cycling stability, the layered/spinel composite is far superior to the single-layered structure. For instance, $NaNi_{1/3}Fe_{1/3}Mn_{1/3}$-$O_2$@NMO-2 retained 85.20% of its initial capacity after 300 cycles at 100 mA g^{-1}, whereas pristine $NaNi_{1/3}Fe_{1/3}Mn_{1/3}O_2$ retained only 61.76% under the same conditions.[123] Similarly, NMNCO-SL achieved 82.5% capacity retention after 280 cycles at 1C, significantly outperforming pristine NMNO (50.4%) and NMNCO-L (55.6%).[145]

Table 2 summarizes the key electrochemical properties (including voltage window, specific capacity, and cycling performance) and phase transitions of the layered/spinel composite structures discussed in this review. Compared with single-phase layered oxides, the composite structures generally

exhibit reversible phase transition pathways. This indicates that introducing the spinel phase helps to buffer structural evolution and suppress irreversible phase transitions. Regarding cycling performance, most of these composite materials can still maintain a capacity retention of over 80–90%, indicating that the 3D ion diffusion channels provided by the spinel structure accelerate Na$^+$ transport kinetics, thereby achieving the synergistic improvement of capacity output and cycling stability.

Although current research has fully demonstrated the superiority of spinel/layered heterostructures, the key to achieving precise design of this strategy lies in establishing selection rules for composition in the spinel phase. Firstly, to enhance interfacial chemical and air stability, TM ions with high TM–O bond energy and a tendency for surface segregation in the layered structure are promising. For example, Ti^{4+} and Cu^{2+} enrich the material surface during high-temperature sintering, forming a dense spinel protective layer,[105,145] which effectively blocks the interlayer insertion of H$_2$O/CO$_2$ molecules and suppresses residual alkali generation. Secondly, to improve the structural stability and suppress phase transitions, ions that can form low total energy spinel phases can be selected. DFT calculations reveal that the introduction of Mg^{2+} lowers the total energy of the MgMn$_2$O$_4$ spinel phase compared to the layered phase.[136] This thermodynamic advantage drives the spontaneous *in situ* precipitation of the spinel phase within the material, providing an intrinsic driving force for the formation of layered/spinel heterostructures.[97] Finally, to accelerate ion transport kinetics, TM ions that can expand the interlayer spacing, such as Mo^{6+}, should be prioritized.[95,123] The Mo^{6+} doping forms a Na$_2$MoO$_4$/spinel/O3 triple-layer heterostructure NFM@NMO-2 that can expand the interlayer spacing and induce surface spinel layer reconstruction.[123] Then, the inherent 3D diffusion framework of the spinel phase and the enlarged interlayer spacing greatly improved the Na$^+$ diffusion rate.

Table 2 Summary of the electrochemical properties and phase transitions of layered/spinel composite materials

Cathode material	Potential window (V)	Capacity (mAh g^{-1}@C)	Phase transition	Cycling	Ref.
1wt%-Co$_x$B@NFM	2–4.3	158.6@0.1	O3 ↔ P3 ↔ OP2	70% (2C, 300 cycles)	109
NFM@NMO-2	2–4.0	161.2@0.1	O3 ↔ P3	85.2% (100 mA g^{-1}, 300 cycles)	123
NaMO-SL	2.2–3.6	180.9@0.1	O3 ↔ P3	79% (1C, 150 cycles)	104
LS-NCM	1.5–4.0	177.6@0.1	O3 ↔ P3	90.6% (0.5C, 400 cycles)	128
LLS-NaNCMM	1.5–4.0	153.8@0.1	P2/P3/spinel ↔ P2/P3″/spine	80.6% (2C, 200 cycles)	121
LLS-NaNCMM15	1.5–4.3	169.4@0.2	P2/P3/spinel ↔ P2/P3″/spinel	65.6% (5C, 100 cycles)	129
LS-NaMM20	2–4.0	187@0.2	P2 ↔ P2′	93 mAh g^{-1} (5C, 500 cycles)	136
NaMCM-700	1.5–4.3	74@5	P3 ↔ O3′	65% (0.1C, 100 cycles)	99
NaMCNB	1.5–4.5	195.7@0.2	P2 ↔ P2	80.1% (0.2C, 100 cycles)	122
NMTN	1.5–4.2	186@0.1	—	81% (5C, 500 cycles)	105
NMNCO-SL	2–4.0	112@0.1	O3 ↔ P3	91.8% (1C, 500 cycles)	145
NFM(OV) + MnFe$_2$O$_4$	1.8–4.2	185.7@0.1	P2 ↔ P′2	82.6% (2C, 300 cycles)	140
P2/P3@spinel-NaMCM	1.5–4.3	135.9@0.1	P2/P3/spinel ↔ P2/P3″/spinel	88.9% (2C, 100 cycles)	107
NNMO	1.5–4.25	178.6@10 mAh g^{-1}	O3/P2/spinel ↔ O3/P2/spinel	86.65% (50 mA g^{-1}, 200 cycles)	98
Na$_{0.5}$Ni$_{1/6}$Co$_{1/6}$Mn$_{2/3}$O$_2$	2.0–4.5	85@10	P2 ↔ O2	60% (C/2, 100 cycles)	93
Na$_{0.72}$Li$_{0.24}$Mn$_{0.76}$O$_2$	1.5–4.5	216.9@0.1	—	130.5 mAh g^{-1} (1C, 100 cycles)	108
LS-NFM	2.0–4.2	112@0.1	O3 ↔ P3	86% (100 mAh g^{-1}, 100 cycles)	95

Despite the significant effectiveness of spinel regulation strategies, several issues still remain. (i) The spinel and layered phases differ in orientation and octahedral connectivity, which can readily generate dislocations and interfacial stress between the two phases and thus weaken stability. By regulating the oxygen partial pressure, sintering temperature, and precursor valence state, local phase transformation can be induced, allowing the spinel phase to be formed only on the surface or grain boundaries. (ii) The balance between spinel content and electrochemical performance is a issue. A spinel coating can protect the layered core against electrolyte corrosion (*e.g.*, HF attack). However, proper spinel phase thickness in composite systems requires rational adjustment. (iii) Limited electrochemical stability. During long-term cycling, the spinel phase may gradually transform into a disordered rock-salt phase, leading to increased interfacial impedance and decreased electrical conductivity. An inert oxide coating can be applied to improve interfacial stability and mitigate side reactions. Meanwhile, such a layer can block oxygen release and electrolyte attack, delaying the disordering process. (iv) Currently, there is no systematic research that elucidates whether specific spinel compositions are inherently more suitable for P2 (hexagonal) or O3 (rhombohedral) lattices in terms of heteroepitaxial growth and strain management. Integrating atomic-scale characterization with first-principles calculations to systematically investigate the relationship between spinel composition, lattice matching, and interfacial strain is a meaningful work as well, which helps to provide a scientific foundation for designing highly stable layered/spinel heterostructures.

To gain an in-depth understanding of the role and mechanism of the spinel phase in the composite configuration and its influence on electrochemical performance, advanced characterization techniques are required (Fig. 15a).[162–164] To the best of our knowledge, conventional characterization methods, such as XRD, SEM, and XPS, can rapidly provide preliminary identification of phases, basic morphology, and surface chemistry.[165–167] However, to capture the key features of
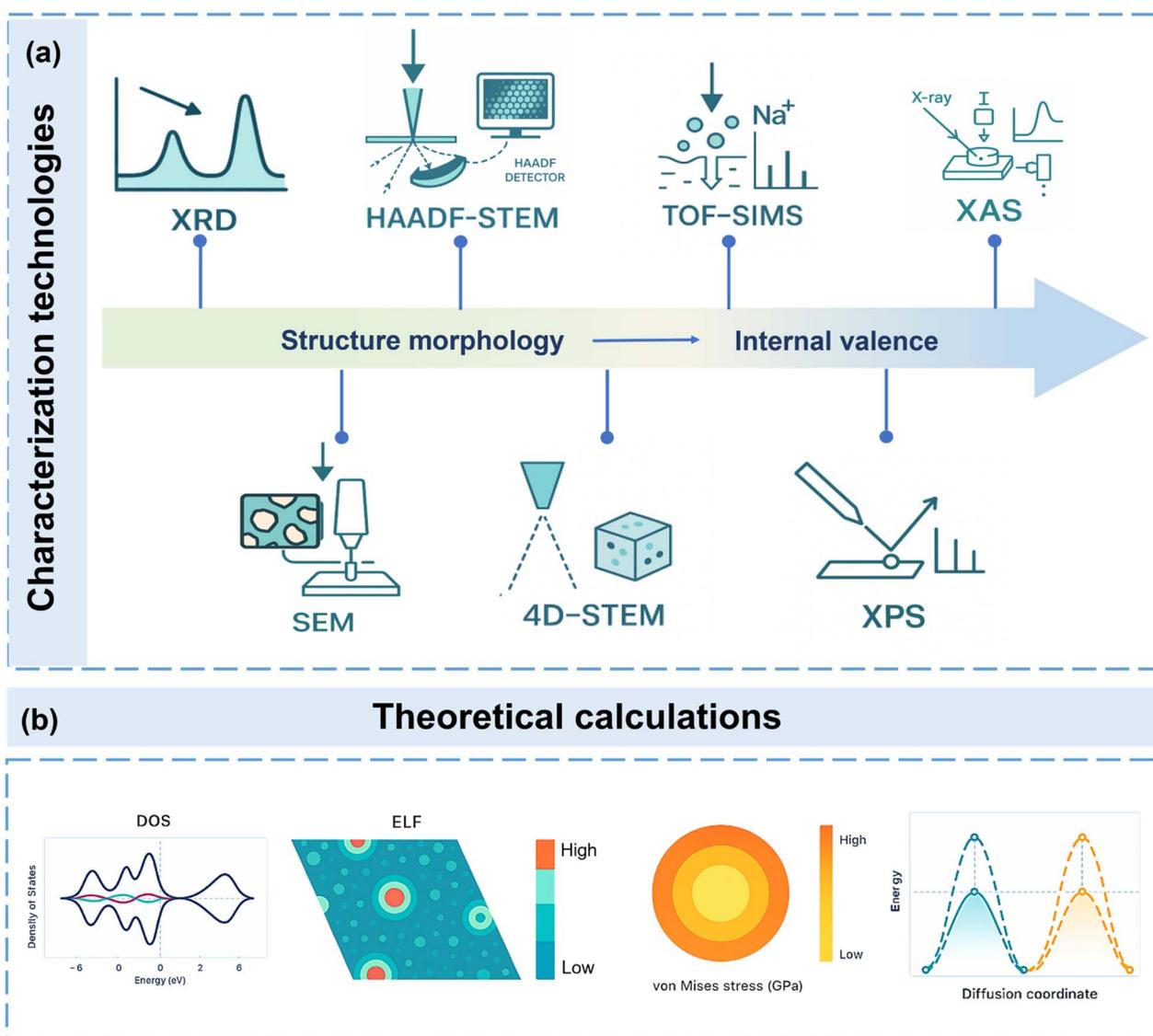

Fig. 15 (a) The promising characterization techniques and (b) theoretical calculations for the development of layered/spinel symbiotic configurations.
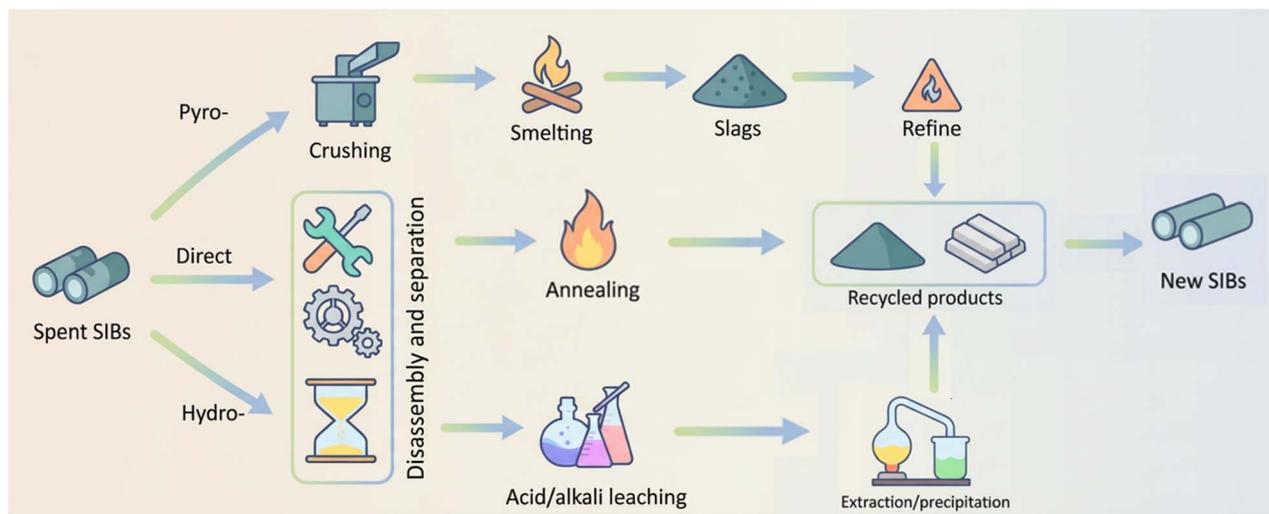
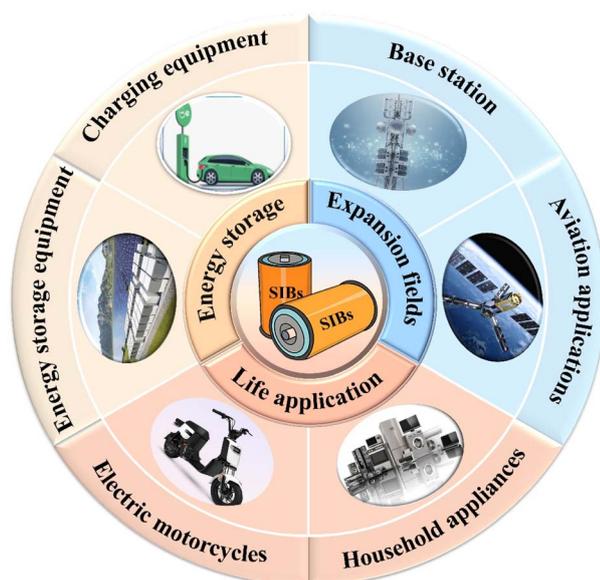Fig. 16 Recycling technologies for layered oxide cathodes.

Fig. 17 The potential application fields of SIBs based on layered/spinel composite cathode.

composite structures, advanced characterization techniques combined with theoretical calculations are required for detailed analysis. HAADF-STEM and four-dimensional scanning transmission electron microscopy (4D-STEM) can capture the dislocations and quantify defect types and densities at the spinel/layered interface, elucidating how these defects affect ionic diffusion and structural stability within the composite structure. Time-of-flight secondary ion mass spectrometry (TOF-SIMS) can reveal the 3D spatial distribution of elements as well as reaction-derived byproduct species.[168] *In situ* synchrotron XAS can probe local structural and electronic state variations of layered oxide cathodes modulated by spinel at the atomic scale, demonstrating the role of the spinel layer in stabilizing TM–O bonds and regulating interfacial charge

transfer.[169–171] On this basis, DFT calculations provide a powerful tool to investigate the electronic structure, chemical bonding, and charge-compensation mechanisms of the material (Fig. 15b).[172,173] Calculation results such as the density of states (DOS), electron localization function (ELF), and migration energy barriers can help elucidate Na^+ migration within the material and provide a theoretical basis for improving its ionic conductivity.[174] Meanwhile, by combining theoretical data such as von Mises stress, the influence of microscopic stress on material performance can be further clarified.[175]

With the continuous expansion of SIB applications, recycling technology has become an indispensable research focus (Fig. 16).[176,177] To date, pyrometallurgy, hydrometallurgy, and direct recycling are the most frequently applied methods for cathode material recycling.[178] Among them, pyrometallurgy involves high-temperature treatment of spent cathode materials, extracting metals through processes such as smelting and roasting.[179] In contrast, hydrometallurgy recovers valuable metals from spent cathodes through hydrochemical processes such as leaching, solvent extraction, and precipitation.[180] Direct recycling restores the functionality of spent cathode materials without completely destroying their structure.[181] For layered/spinel composite structures, the multiphase characteristics pose additional challenges for the recycling process. In both hydrometallurgical and pyrometallurgical processes, the original crystalline structure is completely disrupted, followed by lattice rearrangement, resulting in the formation of metal salts and alloys, respectively.[182–184] In consideration of the higher formation energy of spinel phase and of different elements (like Mo, B),[109,123] the recycling conditions, such as sintering temperature and precipitant, need to be re-evaluated.[185–187] Compared with the high energy consumption of pyrometallurgy, as well as the high pollution and complex processes of hydrometallurgy, direct recycling exhibits significant advantages like simple operation and low energy consumption for the layered/spinel composites.[188–190]

As the advantages of SIBs in terms of cost, safety, and resource sustainability become increasingly evident, their application scenarios are expanding from conventional stationary energy storage toward more diverse and demanding applications. However, different application scenarios impose distinct requirements on cathode materials, particularly with respect to rate capability, cycling stability, and environmental adaptability. Accordingly, spinel regulation strategies are expected to further narrow the gap between laboratory-level performance and practical applications. As shown in Fig. 17, the spinel structure, with its excellent stability and interfacial regulation capability, provides a promising way for future fast-charging SIBs, as it helps mitigate interfacial polarization and structural stress induced by high current densities. Furthermore, the spinel phase also acts as a robust skeleton in the layered/spinel composite oxides, which can greatly enhance the thermal stability of the material. Consequently, spinel-regulated layered oxide cathode materials are not only promising for electric mobility devices and household energy storage systems in daily life, but also well suited for application environments with large temperature fluctuations, such as communication base stations. Moreover, these materials show potential for broader applications in aerospace-related auxiliary power systems and other high-reliability fields. With a deeper understanding of their mechanisms under extreme conditions such as high/low temperatures, and fast charging, spinel regulation can contribute to the development of layered oxides, providing more stable solutions for clean energy and sustainable development.

Author contributions

Rui Li: writing – original draft. Yan-Jiang Li: supervision, writing – review & editing. Neng-Hua Xu: investigation, Bing-Bing Chen: investigation, Hai-Yan Hu: investigation. Yan-Fang Zhu, Yao Xiao: supervision, writing – review & editing.

Conflicts of interest

The authors declare no conflicts of interest.

Data availability

This review is based on previously published data, all of which are cited within the manuscript. No new datasets were generated.

Acknowledgements

References

1 R. A. House, U. Maitra, M. A. Pérez-Osorio, J. G. Lozano, L. Jin, J. W. Somerville, L. C. Duda, A. Nag, A. Walters and K.-J. Zhou, *Nature*, 2020, **577**, 502–508.

2 X.-B. Jia, Q.-Q. Peng, Y.-F. Liu, D.-C. Chen, J. Wang, J.-Y. Li, Y.-F. Zhu, N.-H. Xu, L.-Y. Kong, H.-X. Liu, G.-Y. Zhang, Z.-C. Jian, C. Cheng, H.-H. Dong, L. Zhang, Y. Sun, S.-Q. Chen, X.-D. Guo, S. Dou and Y. Xiao, *Nat. Commun.*, 2025, **16**, 10477.

3 C. Zhao, Q. Wang, Z. Yao, J. Wang, B. Sánchez-Lengeling, F. Ding, X. Qi, X. Lu, X. Bai, B. Li, H. Li, A. Aspuru-Guzik, X. Huang, C. Delmas, M. Wagemaker, L. Chen and Y.-S. Hu, *Science*, 2020, **370**, 708–711.

4 Q. C. Ling, D. C. Chen, X. Zhu, Y. F. Zhu, Z. Z. Hong, J. Liu, Q. Q. Sun, Y. B. Niu, Y. Sun, P. F. Wang and Y. Xiao, *Adv. Mater.*, 2025, **38**, e14352.

5 P. F. Wang, H. Xin, T. T. Zuo, Q. Li, X. Yang, Y. X. Yin, X. Gao, X. Yu and Y. G. Guo, *Angew. Chem., Int. Ed.*, 2018, **57**, 8178–8183.

6 R. Zhang, C. Wang, P. Zou, R. Lin, L. Ma, L. Yin, T. Li, W. Xu, H. Jia, Q. Li, S. Sainio, K. Kisslinger, S. E. Trask, S. N. Ehrlich, Y. Yang, A. M. Kiss, M. Ge, B. J. Polzin, S. J. Lee, W. Xu, Y. Ren and H. L. Xin, *Nature*, 2022, **610**, 67–73.

7 Y. Yang, Z. Wang, C. Du, B. Wang, X. Li, S. Wu, X. Li, X. Zhang, X. Wang, Y. Niu, F. Ding, X. Rong, Y. Lu, N. Zhang, J. Xu, R. Xiao, Q. Zhang, X. Wang, W. Yin, J. Zhao, L. Chen, J. Huang and Y.-S. Hu, *Science*, 2024, **385**, 744–752.

8 G. Y. Zhang, Y. J. Li, H. Y. Hu, Z. Z. Hong, Y. F. Zhu and Y. Xiao, *Adv. Funct. Mater.*, 2025, e20788.

9 X. B. Jia, J. Wang, Y. F. Liu, Y. F. Zhu, J. Y. Li, Y. J. Li, S. L. Chou and Y. Xiao, *Adv. Mater.*, 2023, **36**, 2307938.

10 R. Usiskin, Y. Lu, J. Popovic, M. Law, P. Balaya, Y.-S. Hu and J. N. R. M. Maier, *Nat. Rev. Mater.*, 2021, **6**, 1020–1035.

11 B. Wang, H. A. Doan, S.-B. Son, D. P. Abraham, S. E. Trask, A. Jansen, K. Xu and C. Liao, *Nat. Commun.*, 2025, **16**, 3413.

12 B. Yin, S. Liang, D. Yu, B. Cheng, I. L. Egun, J. Lin, X. Xie, H. Shao, H. He and A. Pan, *Adv. Mater.*, 2021, **33**, 2100808.

13 R. Usiskin, Y. Lu, J. Popovic, M. Law, P. Balaya, Y.-S. Hu and J. Maier, *Nat. Rev. Mater.*, 2021, **6**, 1020–1035.

14 G. Zou, J. Wang, Y. Sun, W. Yang, T. Niu, J. Li, L. Ren, Z. W. Seh and Q. Peng, *Nat. Commun.*, 2025, **16**, 1795.

15 Q. Liu, Z. Hu, W. Li, C. Zou, H. Jin, S. Wang, S. Chou and S.-X. Dou, *Energy Environ. Sci.*, 2020, **14**, 158–179.

16 Y. Xiao, H. R. Wang, H. Y. Hu, Y. F. Zhu, S. Li, J. Y. Li, X. W. Wu and S. L. Chou, *Adv. Mater.*, 2022, **34**, e2202695.

17 P. Zhou, Z. Che, J. Liu, J. Zhou, X. Wu, J. Weng, J. Zhao, H. Cao, J. Zhou and F. Cheng, *Energy Storage Mater.*, 2023, **57**, 618–627.

18 B. S. V. Kausthubharam, A. Sengupta, D. R. Rajagopalan Kannan, V. Premnath, W. S. Tang, J. A. Jeevarajan and P. P. Mukherjee, *ACS Energy Lett.*, 2025, **10**, 5383–5397.

19 Q. Gui, J. Li, B. Jin, P. Liu, K. Yu, J. Zhang and L. Mao, *J. Energy Chem.*, 2025, **112**, 13–28.

20 E. Li, L. Liao, J. Huang, T. Lu, B. Dai, K. Zhang, X. Tang, S. Liu, L. Lei, D. Yin, J. Teng and J. Li, *Energy Storage Mater.*, 2024, **73**, 103805.

21 Z. Liu, M. Zhang, K. Yang, Y. Jin, H. Wang, B. Wei and J. Liu, *e Transportation*, 2025, **26**, 100495.

22 Y. Cao, X. Cao, X. Dong, X. Zhang, J. Xu, N. Wang, Y. Yang, C. Wang, Y. Liu and Y. Xia, *Adv. Funct. Mater.*, 2021, **31**, 2102856.

23 X. He, Y. Ling, Y. Wu, Y. Lei, D. Cao and C. Zhang, *Small*, 2025, **21**, 2412817.

24 Z. Luo, L. Hu, C. Dai, G. Ma, Y. Ye, K. Xu and Z. Lin, *Angew. Chem., Int. Ed.*, 2025, **64**, e202514451.

25 Z.-C. Jian, J.-X. Guo, Y.-F. Liu, Y.-F. Zhu, J. Wang and Y. Xiao, *Chem. Sci.*, 2024, **15**, 19698–19728.

26 H. Liu, L. Kong, H. Wang, J. Li, J. Wang, Y. Zhu, H. Li, Z. Jian, X. Jia, Y. Su, S. Zhang, J. Mao, S. Chen, Y. Liu, S. Chou and Y. Xiao, *Adv. Mater.*, 2024, **36**, 2407994.

27 X. Tan, J. Zeng, L. Sun, C. Peng, Z. Li, S. Zou, Q. Shi, H. Wang and J. Liu, *InfoMat*, 2025, **7**, e12636.

28 J. Liu, N. Zhang, H. Shi, Z. He, Z. Zhang, D. V. Anishchenko, E. V. Alekseeva, R. Li, P. Yang, O. V. Levin, D. Wang, H. Liu, S. Dou and B. Wang, *Chem. Eng. J.*, 2025, **521**, 167111.

29 Q. Liu, Z. Hu, M. Chen, C. Zou, H. Jin, S. Wang, S. L. Chou and S. X. Dou, *Small*, 2019, **15**, 1805381.

30 S. He, R. Zhang, X. Han, Y. Zhou, C. Zheng, C. Li, X. Xue, Y. Chen, Z. Wu, J. Gan, L. She, F. Qi, Y. Liu, M. Zhang, W. Du, Y. Jiang, M. Gao and H. Pan, *Adv. Mater.*, 2025, **37**, 2413760.

31 Y. F. Liu, H. Y. Hu, Y. F. Zhu, D. N. Peng, J. Y. Li, Y. J. Li, Y. Su, R. R. Tang, S. L. Chou and Y. Xiao, *Chem. Commun.*, 2024, **60**, 6496–6499.

32 T. Chen, W. Liu, Y. Zhuo, H. Hu, J. Guo, Y. Liu, J. Yan and K. Liu, *Chem. Eng. J.*, 2019, **383**, 123087.

33 C. Zhao, Z. Yao, Q. Wang, H. Li, J. Wang, M. Liu, S. Ganapathy, Y. Lu, J. Cabana, B. Li, X. Bai, A. Aspuru-Guzik, M. Wagemaker, L. Chen and Y.-S. Hu, *J. Am. Chem. Soc.*, 2020, **142**, 5742–5750.

34 Y. Zhou, M. Sun, M. Cao, Y. Zeng, M. Su, A. Dou, X. Hou and Y. Liu, *J. Colloid Interface Sci.*, 2023, **657**, 472–481.

35 L.-F. Zhou, H. Wang, L. Cao, L.-Y. Liu, H. Jia, Y.-S. Wang and T. Du, *Chem. Eng. J.*, 2025, **526**, 170700.

36 Q.-C. Ling, Q.-Q. Sun, Y.-J. Li, Z.-Z. Hong, H.-S. Xin, X.-Y. Liu, Y.-F. Zhu, S.-X. Dou and Y. Xiao, *Sci. China Chem.*, 2025, **68**, 4068–4090.

37 Q. Wang, D. Zhou, C. Zhao, J. Wang, H. Guo, L. Wang, Z. Yao, D. Wong, G. Schuck, X. Bai, J. Lu and M. Wagemaker, *Nat Sustainability*, 2024, **7**, 338–347.

38 Q. Meng, Y. Huang, L. Li, F. Wu and R. Chen, *Joule*, 2024, **8**, 344–373.

39 X. Liang, T.-Y. Yu, H.-H. Ryu and Y.-K. Sun, *Energy Storage Mater.*, 2022, **47**, 515–525.

40 L. Yao, P. Zou, C. Wang, J. Jiang, L. Ma, S. Tan, K. A. Beyer, F. Xu, E. Hu and H. L. Xin, *Adv. Energy Mater.*, 2022, **12**, 2201989.

41 L. Yu, X. Ma, L. Yang, Q. Guo, S. Ye, N. Ahmad, Z. Jiang, J. Liang, J. Xia, B. Peng, W. He, L. Shi and G. Zhang, *Energy Storage Mater.*, 2025, **83**, 104679.

42 J. Ke and L. Su, *Energy Storage Mater.*, 2025, **76**, 104133.

43 X. Li, S. Yu, X. Zhao and J. Liu, *Energy Storage Mater.*, 2025, **79**, 104303.

44 X. Yang, Y. Li, X. Li, T. Lin, W. Lin, P. Li, D. Xiao, S. Wang and H. Pan, *ACS Energy Lett.*, 2025, **10**, 1491–1498.

45 L.-Y. Kong, H.-X. Liu, Y.-F. Zhu, J.-Y. Li, Y. Su, H.-W. Li, H.-Y. Hu, Y.-F. Liu, M.-J. Yang, Z.-C. Jian, X.-B. Jia, S.-L. Chou and Y. Xiao, *Sci. China Chem.*, 2023, **67**, 191–213.

46 Z. Hong, Z.-C. Jian, Y.-F. Zhu, Y.-J. Li, Q.-C. Ling, H. Xin, D. Wang, C. Wu and Y. Xiao, *Chem. Sci.*, 2025, **16**, 17058–17085.

47 Y. Xiao, Y. F. Liu, H. W. Li, J. Y. Li, J. Q. Wang, H. Y. Hu, Y. Su, Z. C. Jian, H. R. Yao, S. Q. Chen, X. X. Zeng, X. W. Wu, J. Z. Wang, Y. F. Zhu, S. X. Dou and S. L. Chou, *InfoMat*, 2023, **5**, e12475.

48 T. Sheng, L. Wang, H. Nie, Y. Liu, X. Zeng, S. Gan, D. Liu, T. Xie and J. Li, *Adv. Funct. Mater.*, 2025, **35**, 2501688.

49 S. Gao, Y. Huang, J. Geng, W. Hu, K. Feng, J. Zhong, C. Yu and F. Li, *ACS Energy Lett.*, 2025, **10**, 4140–4147.

50 H. Hu, X. Lin, S. Tong, T. Wang, P. Wang, Z. Zhou, X. Yan, M. Jia, Y. Niu and X. Zhang, *Energy Storage Mater.*, 2025, **79**, 104319.

51 Y. Mao, H. Gong, X. Wang, Y. Cao, S. Wang, K. Ma, X. G. Fuku, C. Zhou and J. Sun, *Adv. Energy Mater.*, 2025, **15**, 2502592.

52 J. Wang, D. Chen, H. Dong, Q.-Q. Sun, M.-Y. Li, G.-Y. Zhang, H.-Y. Hu, Y. Pian, J. Yu, Y.-F. Zhu, H. Wei, Y. Sun, S. Zhao, H. Chu, J. Liu and Y. Xiao, *ACS Nano*, 2025, **19**, 31901–31914.

53 A. Langella, A. Massaro, A. B. Muñoz-García and M. Pavone, *ACS Energy Lett.*, 2025, **10**, 1089–1098.

54 J. Dai, J. Li, Y. Yao, Y.-R. Wang, M. Ma, R. Bai, Y. Zhu, X. Rui, H. Wu and Y. Yu, *ACS Nano*, 2025, **19**, 11197–11209.

55 X.-Y. Zhang, L.-Y. Kong, J. Ding, Y.-F. Zhu, J.-Y. Li, Z.-C. Jian, H. Xin, M.-Y. Li, P. Tan, W. K. Pang, S.-X. Dou and Y. Xiao, *ACS Energy Lett.*, 2025, **10**, 2858–2867.

56 Y.-B. Wu, H.-Y. Hu, J.-Y. Li, H.-H. Dong, Y.-F. Zhu, S.-Q. Chen, N.-N. Wang, J.-Z. Wang and Y. Xiao, *Chem. Sci.*, 2025, **16**, 3928–3937.

57 J. Forero-Saboya, Y. Zhou, S. Browne, I. A. Moiseev, C. Pablos, J. Abou-Rjeily, A. Mboup, C. Alphen, L. Zhang, B. Li, A. M. Abakumov, J.-M. Tarascon and S. Mariyappan, *Energy Storage Mater.*, 2025, **80**, 104423.

58 Y.-J. Li, S.-L. Chou and Y. Xiao, *Chin. Chem. Lett.*, 2025, **36**, 110389.

59 X.-Y. Zhang, H.-Y. Hu, X.-Y. Liu, J. Wang, Y.-F. Liu, Y.-F. Zhu, L.-Y. Kong, Z.-C. Jian, S.-L. Chou and Y. Xiao, *Nano Energy*, 2024, **128**, 109905.

60 Z.-C. Jian, W. Shi, Y. Liu, X. Li, J.-Y. Li, Y.-F. Zhu, X. Zhu, Y. Li, P. Tan, P.-F. Wang, S. Chen, S. Zhang, J. Mao, G. Zhou, X.-D. Guo, J. Wang, S. X. Dou and Y. Xiao, *Energy Environ. Sci.*, 2025, **18**, 7995–8008.

61 X. Yang, Y. Li, X. Li, T. Lin, W. Lin, P. Li, D. Xiao, S. Wang and H. Pan, *Energy Storage Mater.*, 2025, **76**, 104158.

62 Y. Sun, H. Wang, D. Meng, X. Li, X. Liao, H. Che, G. Cui, F. Yu, W. Yang, L. Li and Z.-F. Ma, *ACS Appl. Energy Mater.*, 2021, **4**, 2061–2067.

63 K. Kubota and S. Komaba, *J. Electrochem. Soc.*, 2015, **162**, A2538–A2550.

64 Y. F. Liu, K. Han, D. N. Peng, L. Y. Kong, Y. Su, H. W. Li, H. Y. Hu, J. Y. Li, H. R. Wang, Z. Q. Fu, Q. Ma, Y. F. Zhu, R. R. Tang, S. L. Chou, Y. Xiao and X. W. Wu, *InfoMat*, 2023, **5**, e12422.

65 Y.-J. Guo, R.-X. Jin, M. Fan, W.-P. Wang, S. Xin, L.-J. Wan and Y.-G. Guo, *Chem. Soc. Rev.*, 2024, **53**, 7828–7874.

66 H.-R. Yao, P.-F. Wang, Y. Gong, J. Zhang, X. Yu, L. Gu, C. OuYang, Y.-X. Yin, E. Hu and X.-Q. J. J. Yang, *J. Am. Chem. Soc.*, 2017, **139**, 8440–8443.

67 L. Feng, Y. Xia, J. Guo, H. Liu, Y. Hao, Z. Tian, X. Xiao, L. Feng, C. Sun and S. Qi, *Chem. Eng. J.*, 2024, **496**, 154298.

68 Z. Li, W. Xi, Z. Jiang, Y. Zhang, R. Wang, Y. Gong, H. Wang and J. Jin, *Small*, 2025, **21**, e06854.

69 P. Vanaphuti, Z. Yao, Y. Liu, Y. Lin, J. Wen, Z. Yang, Z. Feng, X. Ma, A. C. Zauha and Y. Wang, *Small*, 2022, **18**, 2201086.

70 B. Ouyang, T. Chen, X. Liu, M. Zhang, P. Liu, P. Li, W. Liu and K. Liu, *Chem. Eng. J.*, 2023, **458**, 141384.

71 D. Chen, B. He, S. Jiang, X. Wang, J. Song, H. Chen, D. Xiao, Q. Zhao, Y. Meng and Y. Wang, *Chem. Eng. J.*, 2025, **510**, 161676.

72 M. H. Hassan, J. Fu, J. Liu and E. Detsi, *Mater. Horiz.*, 2025, **12**, 7636–7647.

73 T. Zhang, T. Wang, Y. Zheng, L. Qian, X. Liu, W. Yan and J. Zhang, *Adv. Energy Mater.*, 2025, **15**, e01760.

74 J.-Y. Hwang, S.-T. Myung and Y.-K. Sun, *Chem. Soc. Rev.*, 2017, **46**, 3529–3614.

75 H. Wang, B. Yang, X.-Z. Liao, J. Xu, D. Yang, Y.-S. He and Z.-F. Ma, *Electrochim. Acta*, 2013, **113**, 200–204.

76 Q. Li, Y. Li, M. Liu, Y. Li, H. Zhao, H. Ren, Y. Zhao, Q. Zhou, X. Feng, J. Shi, C. Wu and Y. Bai, *Adv. Mater.*, 2025, **37**, 2415610.

77 Y. Huang, F. Zhang, X. Xu, Y. Wang, P. Sun, K. Jing, F. Wu, Z. An, X. Han, Y. Cao, Y. Liu, X. Liao, Y. Li, Z. Xu and Z. Lu, *Energy Storage Mater.*, 2025, **83**, 104641.

78 W. Zhao, H. Kirie, A. Tanaka, M. Unno, S. Yamamoto and H. Noguchi, *Mater. Lett.*, 2014, **135**, 131–134.

79 M. Xu, G. Gammaitoni, M. Häfner, E. Villalobos-Portillo, C. Marini and M. Bianchini, *Adv. Funct. Mater.*, 2025, 2425499.

80 M. M. Thackeray and K. Amine, *Nat. Energy*, 2021, **6**, 933.

81 Q. Li, Y. Li, Q. Zhou, B. Long, Y. Wang, Y. Li, Z. Qiu, Z. Wang, Y. Zhang, C. Wu and Y. Bai, *Adv. Funct. Mater.*, 2025, e14451.

82 L. Habib, G. Suo, J. Li, C. Lin, X. Luo, G. Yang, Z. K. Kalkozova and K. Naseem, *Energy Storage Mater.*, 2026, **84**.

83 T. H. Vu, L. N. Phan, X. F. Luo, A. Arya, T. Nguyen, J. K. Chang and Y. S. Su, *Small Struct.*, 2025, **6**, 2400623.

84 M. Kitta, R. Kataoka, S. Tanaka, N. Takeichi and M. Kohyama, *ACS Appl. Energy Mater.*, 2019, **2**, 4345–4353.

85 H. Kim, D. Kim and M. Cho, *ACS Appl. Mater. Interfaces*, 2020, **12**, 22789–22797.

86 M. Cui, Y. Zhu, H. Lei, A. Liu, F. Mo, K. Ouyang, S. Chen, X. Lin, Z. Chen and K. Li, *Angew. Chem., Int. Ed.*, 2024, **63**, e202405428.

87 M. Ren, H. Fang, C. Wang, H. Li and F. Li, *Energy Fuels*, 2020, **34**, 13412–13426.

88 B. Put, P. M. Vereecken, N. Labyedh, A. Sepulveda, C. Huyghebaert, I. P. Radu and A. Stesmans, *ACS Appl. Mater. Interfaces*, 2015, **7**, 22413–22420.

89 X. Liu, X. Wang, A. Iyo, H. Yu, D. Li and H. Zhou, *J. Mater. Chem. A*, 2014, **2**, 14822–14826.

90 Z.-Q. Li, Y.-F. Liu, H.-X. Liu, Y.-F. Zhu, J. Wang, M. Zhang, L. Qiu, X.-D. Guo, S.-L. Chou and Y. Xiao, *Chem. Sci.*, 2024, **15**, 11302–11310.

91 A. Medina, C. Pérez-Vicente and R. Alcántara, *Electrochim. Acta*, 2022, **421**.

92 O. K. Park, Y. Cho, S. Lee, H.-C. Yoo, H.-K. Song and J. Cho, *Energy Environ. Sci.*, 2011, **4**.

93 J. Zheng, P. Yan, W. H. Kan, C. Wang and A. Manthiram, *J. Electrochem. Soc.*, 2016, **163**, A584–A591.

94 J. R. Kim and G. G. Amatucci, *Chem. Mater.*, 2015, **27**, 2546–2556.

95 C. Deng, P. Skinner, Y. Liu, R. Hunt, M. L. Lau, M. Sun, C. Ma, W. Tong, J. Xu and H. Xiong, *Chem. Mater.*, 2018, **30**, 8145–8154.

96 X.-J. Nie, X.-T. Xi, Y. Yang, Q.-L. Ning, J.-Z. Guo, M.-Y. Wang, Z.-Y. Gu and X.-L. Wu, *Electrochim. Acta*, 2019, **320**, 134626.

97 Y. Xiao, Y.-F. Zhu, L. Li, P.-F. Wang, W. Zhang, C. Li, S.-X. Dou and S.-L. Chou, *Cell Rep. Phys. Sci.*, 2021, **2**, 100547.

98 Z. Nie, C. Liu, Q.-S. Lai, W. Li, Q. Li, R. Yang, X.-W. Gao, Q. Gu and W.-B. Luo, *Energy Storage Mater.*, 2025, **74**, 103971.

99 J.-Y. Li, H.-Y. Hu, H.-W. Li, Y.-F. Liu, Y. Su, X.-B. Jia, L.-F. Zhao, Y.-M. Fan, Q.-F. Gu, H. Zhang, W. K. Pang, Y.-F. Zhu, J.-Z. Wang, S.-X. Dou, S.-L. Chou and Y. Xiao, *ACS Nano*, 2024, **18**, 12945–12956.

100 H. Y. Hu, Y. F. Zhu, Y. Xiao, S. Li, J. Y. Li, Z. Q. Hao, J. H. Zhao and S. L. Chou, *Adv. Energy Mater.*, 2022, **12**, 2201511.

101 Y.-K. Sun, *ACS Energy Lett.*, 2020, **5**, 1278–1280.

102 X. Liang, X. Song, H. H. Sun, H. Kim, M.-C. Kim and Y.-K. Sun, *Nat. Commun.*, 2025, **16**.

103 J. Y. Li, H. Y. Hu, L. F. Zhou, H. W. Li, Y. J. Lei, W. H. Lai, Y. M. Fan, Y. F. Zhu, G. Peleckis, S. Q. Chen, W. K. Pang, J. Peng, J. Z. Wang, S. X. Dou, S. L. Chou and Y. Xiao, *Adv. Funct. Mater.*, 2023, **33**.

104 M. Tang, J. Yang, H. Liu, X. Chen, L. Kong, Z. Xu, J. Huang and Y. Xia, *ACS Appl. Mater. Interfaces*, 2020, **12**, 45997–46004.

105 S. Guo, Q. Li, P. Liu, M. Chen and H. Zhou, *Nat. Commun.*, 2017, **8**, 135.

106 S. Su, X. Bai, L. Ming, Z. Xiao, C. Wang, B. Zhang, L. Cheng and X. Ou, *J. Solid State Chem.*, 2022, 122916.

107 J. Y. Li, H. Y. Hu, L. F. Zhou, H. W. Li, Y. J. Lei, W. H. Lai, Y. M. Fan, Y. F. Zhu, G. Peleckis, S. Q. Chen, W. K. Pang, J. Peng, J. Z. Wang, S. X. Dou, S. L. Chou and Y. Xiao, *Adv. Funct. Mater.*, 2023, **33**, 2213215.

108 Y. Chen, S. Feng, J. Chen, Y. Lu, M. Wu, X. Wu and Z. Wen, *ACS Appl. Energy Mater.*, 2023, **6**, 12421–12431.

109 S. Feng, Y. Lu, X. Lu, H. Chen, X. Wu, M. Wu, F. Xu and Z. Wen, *Adv. Energy Mater.*, 2024, **14**, 2303773.

110 W. Zuo, A. Innocenti, M. Zarrabeitia, D. Bresser, Y. Yang and S. Passerini, *Acc. Chem. Res.*, 2023, **56**, 284–296.

111 Q. Jiang, X. Li, Y. Hao, J. Zuo, R. Duan, J. Li, G. Cao, J. Wang, J. Wang, M. Li, X. Yang, M. Li, W. Li, Y. Xi, J. Zhang and W. Xiao, *Adv. Funct. Mater.*, 2024, **35**, 2400670.

112 X. Liu, W. Zuo, B. Zheng, Y. Xiang, K. Zhou, Z. Xiao, P. Shan, J. Shi, Q. Li, G. Zhong, R. Fu and Y. Yang, *Angew. Chem., Int. Ed.*, 2019, **58**, 18086–18095.

113 B. Hu, F. Geng, C. Zhao, B. Doumert, J. Trébosc, O. Lafon, C. Li, M. Shen and B. Hu, *ACS Appl. Mater. Interfaces*, 2020, **12**, 41485–41494.

114 G. Qian, H. Huang, F. Hou, W. Wang, Y. Wang, J. Lin, S.-J. Lee, H. Yan, Y. S. Chu, P. Pianetta, X. Huang, Z.-F. Ma, L. Li and Y. Liu, *Nano Energy*, 2021, **84**, 105926.

115 K. Tang, Y. Huang, X. Xie, S. Cao, L. Liu, H. Liu, Z. Luo, Y. Wang, B. Chang, H. Shu and X. Wang, *Chem. Eng. J.*, 2020, **399**, 125725.

116 D. Dai, X. Lai, X. Wang, Y. Yao, M. Jia, L. Wang, P. Yan, Y. Qiao, Z. Zhang, B. Li and D.-H. Liu, *Chin. Chem. Lett.*, 2023, **35**, 109405.

117 X. Lv, Z. Zhang, H. Fei, Y. Gu, X. Xu, H. Wang, Y. Wang, Q. Zhang and H. Liu, *Appl. Phys. A*, 2024, **130**, 653.

118 S. Guo, Y. Sun, P. Liu, J. Yi, P. He, X. Zhang, Y. Zhu, R. Senga, K. Suenaga and M. Chen, *Sci. Bull.*, 2018, **63**, 376–384.

119 J. Liu, W. Huang, R. Liu, J. Lang, Y. Li, T. Liu, K. Amine and H. Li, *Adv. Funct. Mater.*, 2024, **34**, 2315437.

120 T. Chen, C. Wen, C. Wu, L. Qiu, Z. Wu, J. Li, Y. Zhu, H. Li, Q. Kong, Y. Song, F. Wan, M. Chen, I. Saadoune, B. Zhong, S. Dou, Y. Xiao and X. Guo, *Chem. Sci.*, 2023, **14**, 13924–13933.

121 Y. F. Zhu, Y. Xiao, W. B. Hua, S. Indris, S. X. Dou, Y. G. Guo and S. L. Chou, *Angew. Chem., Int. Ed.*, 2020, **59**, 9299–9304.

122 Y. Yang, Y. Feng, Z. Chen, Y. Feng, Q. Huang, C. Ma, Q. Xia, C. Liang, L. Zhou, M. S. Islam, P. Wang, L. Zhou, L. Mai and W. Wei, *Nano Energy*, 2020, **76**, 105061.

123 M. Song, L. Xu, K. Wang, G. Chen, Z. Tang, K. Zhou, W. Wu and X. Wu, *J. Colloid Interface Sci.*, 2025, **684**, 148–158.

124 W. Su, H. Song, H. Mao, D. Wang, Y. Liu, D. Xiao, Y. Lyu and B. Guo, *Chem. Eng. J.*, 2023, **475**, 146350.

125 W. Huang, X. Li, W. Zhao, C. Zhu, H. Ren, H. Chen, F. Pan and M. Zhang, *Nano Energy*, 2022, **96**, 107092.

126 L. Wang, B. Zhu, D. Xiao, X. Zhang, B. Wang, H. Li, T. Wu, S. Liu and H. Yu, *Adv. Funct. Mater.*, 2023, **33**, 2212849.

127 W. Song, D. Lu, H. Yu, P. Xiao, X. Shi, L. Zuo, X. Yun, C. Zheng and Y. Chen, *Adv. Funct. Mater.*, 2025, e16549.

128 P. Hou, J. Yin, X. Lu, J. Li, Y. Zhao and X. Xu, *Nanoscale*, 2018, **10**, 6671–6677.

129 H. Y. Hu, Y. F. Zhu, Y. Xiao, S. Li, J. Y. Li, Z. Q. Hao, J. H. Zhao and S. L. Chou, *Adv. Energy Mater.*, 2022, **12**, 2201511.

130 S. Feng, C. Zheng, Z. Song, X. Wu, M. Wu, F. Xu and Z. Wen, *Chem. Eng. J.*, 2023, **475**, 146090.

131 F. Ding, C. Zhao, D. Xiao, X. Rong, H. Wang, Y. Li, Y. Yang, Y. Lu and Y.-S. Hu, *J. Am. Chem. Soc.*, 2022, **144**, 8286–8295.

132 M. Yoon, Y. Dong, J. Hwang, J. Sung, H. Cha, K. Ahn, Y. Huang, S. J. Kang, J. Li and J. Cho, *Nat. Energy*, 2021, **6**, 362–371.

133 C. Xu, Y. Ma, J. Zhao, P. Zhang, Z. Chen, C. Yang, H. Liu and Y. S. Hu, *Angew. Chem., Int. Ed.*, 2023, **135**.

134 W. Wang, Y. Sun, P. Wen, Y. Zhou and D. Zhang, *J. Energy Storage*, 2023, **79**, 110177.

135 Z. Qing, H. Zou, X. Zhou, H. Li and Y. Li, *Ceram. Int.*, 2023, **49**, 37800–37807.

136 Y. Xiao, Q. Q. Sun, D. Chen, J. Wang, J. Ding, P. Tan, Y. Sun, S. Zhang, P. F. Wang, J. Mao and Y. F. Zhu, *Adv. Mater.*, 2025, **37**, 2504312.

137 L. Feng, J. Guo, C. Sun, X. Xiao, L. Feng, Y. Hao, G. Sun, Z. Tian, T. Li, Y. Li and J. Yinzhu, *Small*, 2024, **20**, 2403084.

138 M. Yang, S. Zhao, P. Guo, M. Cui, H. Li, M. Wang, J. Wang, F. Wu and G. Tan, *Energy Storage Mater.*, 2025, **78**, 104272.

139 Y. Li, L. Lei, J. Hou, G. Wang, Q. Ren, Q. Shi, J. Wang, L. Chen, G. Zu and S. Li, *J. Energy Chem.*, 2025, **105**, 224–232.

140 Y. Wang, Z. Sun, J. Jin, X. Zhao, X. Qu, L. Jiao and Y. Liu, *Adv. Funct. Mater.*, 2025, **35**, 2504354.

141 B. S. Kumar, A. Pradeep, V. Srihari, H. K. Poswal, R. Kumar, A. Amardeep, A. Chatterjee and A. Mukhopadhyay, *Adv. Energy Mater.*, 2023, **13**, 2204407.

142 H.-R. Yao, X.-G. Yuan, X.-D. Zhang, Y.-J. Guo, L. Zheng, H. Ye, Y.-X. Yin, J. Li, Y. Chen, Y. Huang, Z. Huang and Y.-G. Guo, *Energy Storage Mater.*, 2022, **54**, 661–667.

143 J.-Y. Hwang, S.-T. Myung, J. U. Choi, C. S. Yoon, H. Yashiro and Y.-K. Sun, *J. Mater. Chem. A*, 2018, **5**, 23671–23680.

144 Y. Yu, W. Kong, Q. Li, D. Ning, G. Schuck, G. Schumacher, C. Su and X. Liu, *ACS Appl. Energy Mater.*, 2020, **3**, 933–942.

145 M. Li, H. Zhuo, M. Song, Y. Gu, X. Yang, C. Li, Z. Liao, Y. Ye, C. Zhao, Y. Jiang, J. Liang, D. Wang, K. Wang, D. Geng and B. Xiao, *Nano Energy*, 2024, **123**.

146 Q. Liu, Y.-H. Feng, X. Zhu, M. Liu, L. Yu, G.-X. Wei, X.-Y. Fan, X. Ji, P.-F. Wang and H. Xin, *Nano Energy*, 2024, e109389.

147 M. Li, C. Sun, R. Zhang, M. Qi, Z. Wu, X. Zhang, Y. Zhang, J. Yuan and N. Zhang, *Adv. Mater.*, 2025, e10882.

148 P. Barnes, K. Smith, R. Parrish, C. Jones, P. Skinner, E. Storch, Q. White, C. Deng, D. Karsann, M. L. Lau, J. J. Dumais, E. J. Dufek and H. Xiong, *J. Power Sources*, 2019, **447**, 227363.

149 D. M. C. Ould, S. Menkin, H. E. Smith, V. Riesgo-Gonzalez, E. Jónsson, C. A. O'Keefe, F. Coowar, J. Barker, A. D. Bond, C. P. Grey and D. S. Wright, *Angew. Chem., Int. Ed.*, 2022, **61**, e202202133.

150 Y. F. Liu, H. X. Liu, Y. F. Zhu, H. R. Wang, J. Y. Li, Y. C. Li, H. Y. Hu, Z. G. Wu, X. D. Guo and Y. Xiao, *Adv. Mater.*, 2025, **37**, 2417540.

151 G. Zou, C. Wang, H. Hou, C. Wang, X. Qiu and X. Ji. *Small*, 2017, **13**, 1700762.

152 H. Liu, H. Guo, B. Liu, M. Liang, Z. Lv, K. R. Adair and X. Sun, *Adv. Funct. Mater.*, 2018, **28**, 1707480.

153 Y. J. Li, Y. F. Zhu, B. B. Chen, X. B. Jia, H. Xin, G. Z. Zhao, G. Zhu, S. X. Dou and Y. Xiao, *Adv. Funct. Mater.*, 2025, **35**, 2504096.

154 Z. Cui, Q. Li, S. Li, W. Zheng, X. Li, D. Shu, L. Yuan, J. Lu, H. Cheng and T. Meng, *Small*, 2025, **21**, 2410766.

155 D. Wang, Z. Wu, W. Xiang, Y. Liu, G. Wang, K. Hu, Q. Xu, Y. Song and X. Guo, *J. Energy Chem.*, 2021, **64**, 344–353.

156 R. Kataoka, T. Kojima, M. Kitta and A. Machida, *J. Alloys Compd.*, 2021, **890**, 161763.

157 Z. Shao, X. Wu, X. Wu, S. Feng and K. Huang, *Mater. Chem. Front.*, 2023, **7**, 5288–5308.

158 I. Moeez, D. Susanto, J. H. Park, J. Y. Kim, H. D. Lim and K. Y. Chung, *Adv. Funct. Mater.*, 2023, **33**, 2210370.

159 A. Chiring and P. Senguttuvan, *Bull. Mater. Sci.*, 2020, **43**, 306.

160 B. Su, H. Liang, X. Zhao, T. Zhang, Y. Zhou and D. Y. W. Yu, *Electrochim. Acta*, 2022, **440**, 141746.

161 J. Guo, J. Zheng, W. Zhou, X. Long, X. Zhou, W. Cha, L. Feng, Y. Hao, W. Ni and Y. Li, *Adv. Funct. Mater.*, 2025, **35**, 2500604.

162 Z. Shadike, E. Zhao, Y. N. Zhou, X. Yu, Y. Yang, E. Hu, S. Bak, L. Gu and X. Q. Yang, *Adv. Energy Mater.*, 2018, **8**, 1702588.

163 Y. Liu, J. Li, Q. Shen, J. Zhang, P. He, X. Qu and Y. Liu, *eScience*, 2022, **2**, 10–31.

164 K. Zaghib, M. Armand and M. Gauthier, *J. Electrochem. Soc.*, 1998, **145**, 3135.

165 A. V. Llewellyn, A. Matruglio, D. J. L. Brett, R. Jervis and P. R. Shearing, *Condens. Matter*, 2020, **5**.

166 O. Klvač, D. Trochta, L. Novák, P. Priecel, M. Bornhöfft, T. Kazda and Z. Liu, *Energy Storage Mater.*, 2025, **81**.

167 F. Zhang, Y. Li, B. Ding, G. Shao, N. Li and P. Zhang, *Small*, 2023, **19**, e2303867.

168 S. Sukumaran, S. Fearn and S. J. Skinner, *Cell Rep. Phys. Sci.*, 2025, **6**, 102447.

169 Z. Wu, W. Kong Pang, L. Chen, B. Johannessen and Z. Guo, *Batteries Supercaps*, 2021, **4**, 1547–1566.

170 Y. Fan, X. Wang, G. Bo, X. Xu, K. W. See, B. Johannessen and W. K. Pang, *Adv. Sci.*, 2025, **12**, 2414480.

171 Q. Gu, J. A. Kimpton, H. E. Brand, Z. Wang and S. Chou, *Adv. Energy Mater.*, 2017, **7**, 1602831.

172 J. A. K. Satrughna, A. Kanwade, A. Srivastava, M. K. Tiwari, S. C. Yadav, S. T. Akula and P. M. Shirage, *Mater. Today*, 2023, **91**, 375–408.

173 M. Yang, S. Chen, Y. Jia and L. Ouyang, *Mater. Sci. Eng.: R: Rep.*, 2026, **167**, 101097.

174 Q. Bai, L. Yang, H. Chen and Y. Mo, *Adv. Energy Mater.*, 2018, **8**, 1702998.

175 X. Jin, M. Pei, D. Liu, Z. Song, W. Jiang, R. Mao, B. Li, X. Jian and F. Hu, *Energy Environ. Sci.*, 2024, **17**, 7035–7046.

176 H. Rostami, J. Valio, P. Suominen, P. Tynjälä and U. Lassi, *Chem. Eng. J.*, 2024, **495**, 153471.

177 Y. Zhao, Y. Kang, J. Wozny, J. Lu, H. Du, C. Li, T. Li, F. Kang, N. Tavajohi and B. Li, *Nat. Rev. Mater.*, 2023, **8**, 623–634.

178 G. Ji, J. Wang, Z. Liang, K. Jia, J. Ma, Z. Zhuang, G. Zhou and H. M. Cheng, *Nat. Commun.*, 2023, **14**, 584.

179 Z. Lu, L. Ning, X. Zhu and H. Yu, *Materials*, 2025, **18**, 2987.

180 Y. Lan, X. Li, G. Zhou, W. Yao, H. M. Cheng and Y. Tang, *Adv. Sci.*, 2024, **11**, 2304425.

181 S. A. Ali, S. Zafar, I. Sadiq and T. Ahmad, *Small*, 2025, **21**, e10142.

182 M. Huang, M. Wang, L. Yang, Z. Wang, H. Yu, K. Chen, F. Han, L. Chen, C. Xu, L. Wang, P. Shao and X. Luo, *Nano Micro Lett.*, 2024, **16**, 207.

183 L. L. Driscoll, A. Jarvis, R. Madge, E. H. Driscoll, J.-M. Price, R. Sommerville, F. S. Tontini, M. Bahri, M. Miah, B. L. Mehdi, E. Kendrick, N. D. Browning, P. K. Allan, P. A. Anderson and P. R. Slater, *Joule*, 2024, **8**, 2735–2745.

184 L. Brückner, J. Frank and T. Elwert, *Metals*, 2020, **10**, 1107.

185 Q. Liu, Y. Li, Y. Su, Y. Fan, F. Hu, C. Li, L. Tian, Y. Luo, B. Cao and L. Xu, *Nano Research Energy*, 2025, **5**, e9120177.

186 C. Li, W. Zeng, J. Wang, Z. Li, J. Zhang, X. Wang and S. Mu, *Mater. Horiz.*, 2025, DOI: 10.1039/d4mh01803f.

187 Y. Wang, E. Goikolea, I. R. de Larramendi, S. Lanceros-Méndez and Q. Zhang, *J. Energy Storage*, 2022, **56**, 106053.

188 S. A. Ali, S. Zafar, I. Sadiq and T. J. S. Ahmad, *Small*, 2025, **21**, e10142.

189 T. Liu, Y. Zhang, C. Chen, Z. Lin, S. Zhang and J. J. N. c. Lu, *Nat. Commun.*, 2019, **10**, 1965.

190 Y. Hao, J. Guo, W. Liu, X. Zhou, Z. Tian, Z. Zhang, Y. Li, X. Zhang and Y. Jiang, *ACS Nano*, 2025, **19**, 4496–4504.